UNIVERSIDAD AUTÓNOMA DE MADRID (UAM)
DEPARTAMENTO DE FÍSICA TEÓRICA

Calculation of the Optimal Filtering Coefficients and check of the signal reconstruction for the ATLAS Electromagnetic Calorimeter

Ph.D. DEA: **Carolina Gabaldón Ruiz**
Supervisor: **Dr. Jose Del Peso Malagón**

Agradecimientos

Este trabajo no se habría podido realizar sin la colaboración de muchas personas que me han brindado su ayuda, sus conocimientos y su apoyo. Quiero agradecerles a todos ellos cuanto han hecho por mí, para que este trabajo saliera adelante de la mejor manera posible.

En primer lugar, quiero expresar mi agradecimiento a mi tutor Jose del Peso. Gracias Jose porque sin ti no hubiera sobrevivido en el CERN, has sabido dirigir mi trabajo en estos dos años y enfocarlo con éxito. He aprendido contigo que si quieres algo lo puedes conseguir, solo tienes que esforzarte.

De igual manera, mi más sincero agradecimiento al director del grupo Fernardo Barreiro a quien debo el realizar el doctorado en el grupo de Altas Energías de la Universidad Autónoma de Madrid. Gracias por la confianza que has depositado en mi y por tu interés por mi trabajo.

A Eduardo le agradezco profundamente su apoyo en los momentos difíciles. Gracias por estar siempre dispuesto a ayudarme en el trabajo y en la vida. Ha sido un placer compartir el tiempo de la universidad y de estos dos años de doctorado contigo.

A toda la gente del grupo de Altas Energías, gracias por haberme aceptado como parte del grupo. En particular, muchas gracias a Luis Labarga por haber podido contar con sus conocimientos de física y por las charlas mantenidas. A todos los del laboratorio, por su paciencia conmigo en el campo de la informática y como amigos.

Un mención especial a Pascal Pralavorio que me ha ayudado en el CERN y me han enseñado realmente ha apreciar la física y ha creer que podriamos realizar un buen trabajo. Gracias por formar un equipo conmigo.

Agradecer hoy y siempre a mi familia, mi madre y mi hermano, los tres formamos un equipo. Mama gracias porque sin ti no habría podido empezar, ni terminar la carrera y porque siempre has estado conmigo en los malos y buenos momentos. Y a Nicola porque tiene la facultad de convertir todas las cosas malas en buenas y porque siempre está a mi lado.

Contents

Chapter 1

Introduction

In the 20th century, particle physics experiments have proven crucial for our understanding of nature. Particle accelerators like the Large Hadron Collider (LHC) boost subatomic particles to nearly the speed of light, before letting them collide. The extreme energy densities in these collisions are similar to those that existed just after the Big Bang, when the universe was created. Hence, the LHC results may give some lights on the understanding of the early stages of the Universe.

The particles that are created in the collisions are detected by a particle detector. These detectors are extraordinarily complex, requiring years of research and development. The work of the present "tesina" is related to one of the general purpose LHC experiments, ATLAS, and in particular, it is about the calibration of the liquid Argon Electromagnetic Calorimeter using cosmic muon data.

The EM calorimeter is installed in the ATLAS cavern since the end of 2006. Before the LHC start, the main challenge is to operate coherently its $\sim 170\,000$ channels, which implies the commission of the associated electronics, the determination of the calibration constants, the reconstruction of the signal amplitude from a digital filtering technique (Optimal Filtering Method) and the development of automation algorithms among other tasks.

Many of the physics process to be measured in ATLAS from proton-proton collision will have electrons or photons in the final state. $Higgs \rightarrow \gamma\gamma$, $Higgs \rightarrow e^+e^-e^+e^-$ or $Z' \rightarrow e^+e^-$ are some examples among them. The measurement of the energy and direction of these final state particles put strict requirements in the construction and calibration of the Electromagnetic Calorimeter. In particular a very good signal reconstruction, at the level of 1%, is demanded.

The signal reconstruction method, adopted for the ATLAS Electromagnetic Calorimeter, is based on an accurate knowledge of the calorimeter cells properties and the elec-

tronic chain characteristics [11]. It has been checked and tuned in the past using electrons beams of known energy for the Electromagnetic Barrel (EMB) Calorimeter [12, 14]. In this ”tesina” the signal reconstruction method is applied for the first time to the End-Cap Electromagnetic Calorimeter (EMEC) and tested using cosmic muon data.

At present, cosmic muons are the only possible real data before the starting of the LHC. They have been used recently for doing some uniformity studies and timing performance in the EMB Calorimeter [15]. Other sub-detectors operational in the ATLAS pit can be used as trigger for these muons. In particular, in the present work the trigger was defined by the Hadronic Tile Calorimeter (TileCal), which surrounds the EMB and EMEC calorimeters. In contrast to the EMB calorimeter, the muons entering the EMEC are not projective to the nominal ATLAS center (or nominal interaction point). As a consequence only muon events with high energy deposits, for instance those which radiate a bremsstrahlung photon in their way through the calorimeter, produce a detectable signal in the EMEC. The photon generates an electromagnetic cascade at a certain location inside the calorimeter with enough energy deposition for the purpose of the present studies. The number of such muons is however a small fraction of the total triggered by the TileCal. These events are selected and analysed in both parts EMB and EMEC for the first time.

The EMEC, much less tested so far, will have the main focus in this analysis. However, a detailed comparison between EMEC and EMB is also provided, which is particularly important as: (i) the same reconstruction scheme will be applied for the barrel and the end-cap parts; (ii) the geometry of the latter is more complicated than the former with the consequence that most electrical parameters vary by a factor $2-3$ over the end-cap η-coverage, whereas they are almost constant in the barrel part. This requires intensive cross-checks to avoid any systematic bias.

Although the emphasis in this document will be put in the analysis of the cosmic muon data to check the signal reconstruction method in the EMEC, the work has also involved the production of all calibration constants for the EMEC, for its more than 60,000 cells or channels. In particular all the predicted physics pulse shape and Optimal Filtering Coefficients have been computed and recorded in the Conditional Data Base for use in any physics analysis by any member of ATLAS.

The outline of this ”tesina” is as follows. In Chapter 2 an overview of the ATLAS experiment is given. Chapter 3 recalls the main characteristics and specificities of the EM calorimeter. Chapter 4 describes the algorithms used to the reconstruction of the signal in the EM calorimeter. Chapter 5 details the inputs needed for the signal reconstruction and estimates the calibration bias and the noise reduction linked to the method. In Chapter 6 some generalities about cosmic muons and the ATLAS setup for the muon tests are covered. Chapter 7 gives the results of the quality checks performed with the cosmic muon data. Finally, Chapter 8 is dedicated to conclusions.

Chapter 2

LHC machine and ATLAS detector

2.1 LHC

The Large Hadron Collider(LHC) [1] will become CERN's main accelerator complex. It is currently under construction in the same tunnel that was used for LEP accelerator, which was decommissioned in 2000. The LHC will accelerate two counter-rotating protons beams to an energy of 7 TeV, which will collide head-on at four points along the ring. The resulting interactions have an unprecedented center of mass energy of 14 TeV, which will allow physicist to study new field of physics. The startup is scheduled for summer 2008.

The acceleration of the protons starts at a dedicated linear accelerator (linac), which accelerates bunches of 10^{11} protons to an energy of 50 Mev. These bunches are then transferred to the PS Booster (PSB), where the energy is increased to 1.4 GeV. The energy is further increased to 26 GeV by the Proton Synchrotron (PS). The protons are then injected into the Super Proton Synchrotron (SPS) where they are accelerated to 450 GeV. Finally, the SPS injects the protons clockwise and counter-clockwise into the LHC ring, where they are accelerated to their final energy of 7 TeV. More than 1200 dipole magnets are installed along the LHC ring to keep the protons on track in the ring. The dipoles provide a magnetic field of up to 9 Tesla. The main parameters of the LHC accelerator are given in table 2.1.

Like its center of mass energy, the luminosity of the LHC is also unprecedented for a proton collider. The luminosity is defined as the number of protons that pass by, per unit area, per unit time. The higher the luminosity, the more proton-proton interactions per second will occur. At the LHC design luminosity of 10^{34} $\mathrm{cm}^{-2}\mathrm{s}^{-1}$, on average about 27 interaction will occur per bunch crossing, with a bunch spacing of 25 ns. Thus the number of proton-proton interactions per second will be around 10^9. Such high luminosity is

needed because many interesting physics processes at the LHC energy have very small cross section, 1 pb or less (1 pb=10^{-36} cm^2).

Parameter	Value	Unit
Circumference	26659	m
Beam energy	7	TeV
Injection energy	0.45	TeV
Dipole field at 450 GeV	0.535	T
Dipole field at 7 TeV	8.33	T
Helium temperature	1.9	K
Coil aperture	56	mm
Distance between apertures	194	mm
Luminosity	10^{34}	$cm^{-2}s^{-1}$
Luminosity lifetime	10	h
Bunch spacing	25	ns
Particles per bunch	10^{11}	
Bunches per beam	2808	

Table 2.1: *Main LHC parameters*

Four detectors are under construction at the points where the beams collide: ALICE, ATLAS,CMS and LHCb. ATLAS and CMS are general purpose detectors, i.e. they are designed to cover a wide range of physics. Their primary task will be to discover the Higgs particle (if it exist), but they will also explore the physics beyond the Standard model, like supersymmetry, extra dimension, and even mini black holes. The ATLAS experiment is described in more detail in the next section.

The LHCb experiment is dedicated to the study of CP-violation in the B-system,it is therefore optimized for the detection of B-mesons. LHC uses a low luminosity beam of about 10^{32} cm^{-2}s^{-1}, by defocusing the proton beams near the interaction point. This is needed because the production and decay vertices of the B-mesons are difficult to reconstruct if there is more than one interaction per bunch crossing.

The ALICE experiment focus on the study of the quark-gluon plasma, by measuring the particles that are produced in heavy ion collisions. The quark-gluon plasma is a hadronic state where quarks and gluons are not in bound state like protons anymore, but move freely in the plasma. It is expected that the extreme energy densities in the heavy ion collision is sufficient to create this state of matter for a fraction of a second.

2.2 The ATLAS experiment

The ATLAS detector is currently under assembly at 'point 1', the interaction point near the CERN Meyrin site. Like most colliding beam experiments it has approximate cylindrical symmetry. The detector is organized in a central barrel where the detection elements form cylindrical layers around the beam pipe, and two end-caps organized in cylindrical wheels. Figure 2.1 gives an overall view of the detector.

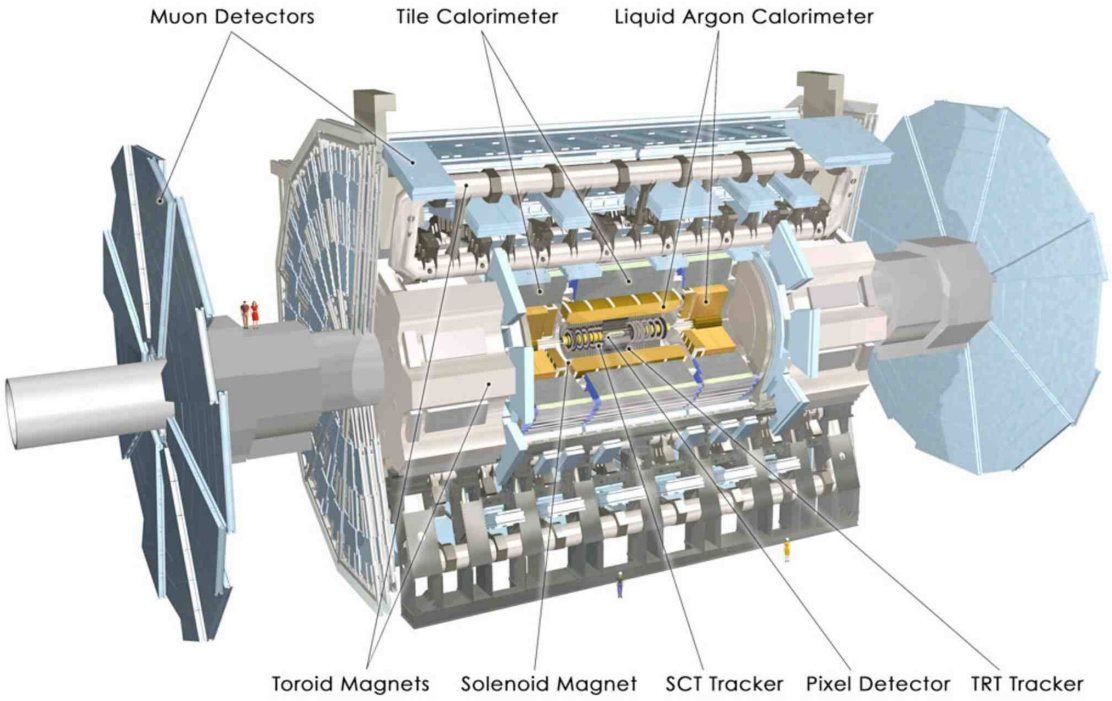

Figure 2.1: *Overview of the ATLAS detector. The various subsystems have been indicated*

The cylindrical symmetry makes a polar coordinate system useful. The direction of the proton beams is the z-axis, being zero the ATLAS center or nominal interaction point and positive z values corresponds to the side where the End-Cap A is located. The origin for the azimuthal angle (Φ) points to the center of the LHC ring (x-axis), while the origin of the polar angle θ is the positive z-axis. Instead of the polar angle θ, the pseudorapidity $\eta = -log(tan(\theta/2))$ is used. The pseudorapidity is a convenient quantity because the particle multiplicity is approximately constant as a function of η. The name comes from the fact that the pseudorapidity of a particle in the massless limit is equal to the rapidity $y = \frac{1}{2} log \frac{E+p_z}{E-p_z}$.

ATLAS consist of three subsystems. The inner-most system is the inner detector, which detects the track of changed particles. The energy of the particles and jets are measured by the calorimeters, which are built around the inner detector. And in the outer-most

part, the muon spectrometer to detect the muons, which scape the calorimeters. ATLAS is 45 meters long and 22 meters high, which makes its volume an order of magnitude larger than previous collider experiments. This is a direct consequence of the 14 TeV center of mass energy of the LHC beams. The large volume give the trackers a long level arm, which improve the momentum resolution, particularly at high momenta. Thick calorimeters are required to fully contain the shower in the calorimeter, and reduce the amount of punch-through into the muon chambers to a minimum. Fast electronics are required to "keep up" with the bunch crossing rate, which is also higher than in previous experiments.

A large number of particles is expected to be produced in the proton collisions. Many of those particles are grouped into jets. Since jets often have a large boost, the particles in a jet are nearly collinear. A detector with fine granularity is required to distinguish particles within a jets. Since the particle flux decreases as a $\frac{1}{R^2}$, the requirement of granularity become less important for the detector elements that are further away from the interaction point.

The basic design criteria of the ATLAS detector are:

- Very good electromagnetic calorimeter for electron and photon identification and energy measurement, complemented by full-coverage hadronic calorimetry for accurate jet and missing traverse-energy measurements;
- High-precision muon momentum measurements, with the capability of guarantee accurate measurements at high luminosity using the external muon spectrometer;
- Efficient tracking at high luminosity for momentum measurement of high p_T leptons, electron identification, τ-lepton and heavy-flavor identification, and full event-reconstruction capability.
- Large acceptance in pseudo-rapidity with almost full azimuthal angle coverage everywhere.
- Triggering and measurements of particles at low-p_T threshold, providing high efficient for most physics processes at LHC.

2.2.1 Inner Detector

The Inner Detector(ID) system [2] covers the acceptance range $|\eta| < 2.5$, matching that of the rest of the ATLAS sub-detectors for precision physics. The ID, thanks to the tracks bending provided by the solenoid magnet, is responsible to measure the momentum of the charged particles coming from the interaction point. Together with the electromagnetic calorimeter, it provides the identification of electrons and photons. Its tracking capability allows to reconstruct secondary vertex from the decay of τ leptons and b-flavored hadrons.

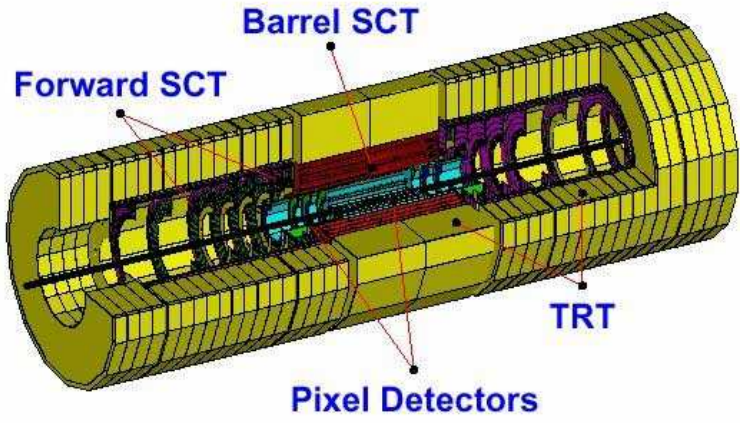

Figure 2.2: *Tridimensional cut-away view of the ATLAS inner detector system*

The ATLAS ID tracking system (figure 2.2) is composed of three different subdetectors layers:

- **The Pixel Detector (PD)** is a finely segmented silicon detector located in the radial range between 4 and 22 *cm* from the beam line. The PD is composed of 3 different layers, located at increasing radio and designed to give 3 space points per track. The first pixel layer gives a substantial contribution to the secondary vertex measurements, and is designed to be replaceable due to the very hostile radiation environment.

- **The Semiconductor Tracker (SCT)** is a silicon detector located in the radial range between 22 and 56 *cm*. It is divided in barrel and end-cap parts. The barrel uses 4 layers of silicon micro-strips to provide precision points in space.

- **Transition Radiation Tracker(TRT)** is based on the use of straw tubes that can operate at very high rate. The straw tubes are filled with a gas mixture $X_e/CO_2/O_2$. The straws are interleaved with polypropylene foils for the identification of electrons through the transition radiation effect.

2.2.2 The calorimeters

The calorimetry system in the ATLAS detector identifies and measures the energy of particles (both charged and neutral) and jets. It also detects missing transverse energy by summing all the measured energy deposit: $E_T^{miss} = \sqrt{(\sum E_T cos\phi)^2 + (\sum E_T sin\phi)^2}$, where $E_T = E_{cell}\ cos(\theta_{cell})$.

The calorimeters contain dense materials (absorber), which cause an incoming particle to initiate a shower. Particles that are created in this shower are detected in the active material, which is interleaved with the absorbers. The total signal in the active material is proportional to the energy of the incoming particle. ATLAS uses two types of active material: liquid argon (LAr) and scintillating plastic. Charged particles that traverse the liquid argon create charge by ionization, which is collected on readout electrodes. The scintillating plastic is doped with fluorescent dye molecules, which emit light when the atoms in the plastic are excited by the crossing of a charged particle. This light is detected and amplified by photomultiplier tubes. For the absorbers several different types of material are used, depending on factors like space constraints and ease of manufacturing: lead, iron, copper and tungsten. The location of the calorimeters is shown in figure 2.3. The pseudorapidity coverage by the whole calorimetry system is $|\eta| \leq 4.9$.

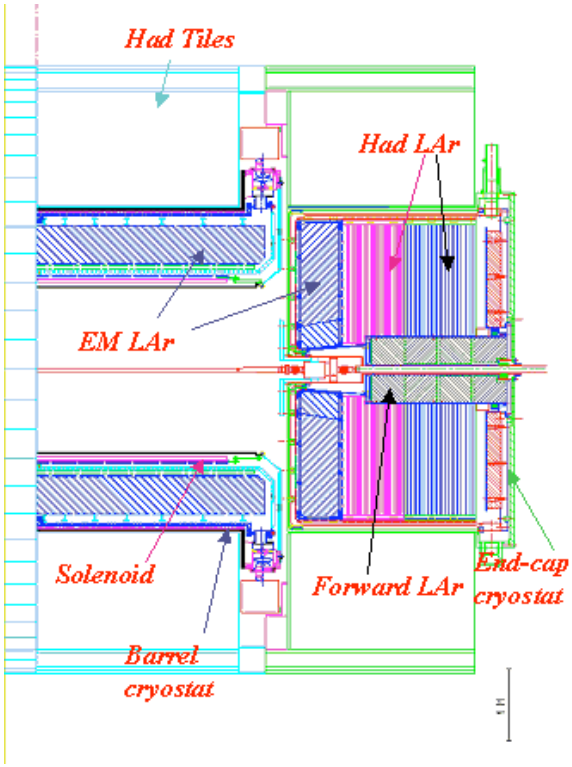

Figure 2.3: *Right side's schematic view of the calorimeter systems in ATLAS.*

The electromagnetic calorimeter

The electromagnetic calorimeter [3] identifies electrons and photons and measures their energy. It consists of a barrel ($0 < |\eta| < 1.475$) and two end-caps ($1.375 < |\eta| < 3.2$). It uses liquid argon as the active medium and lead absorber plates as the passive medium.

The lead plates are folded into an accordion shape. This configuration prevents cracks along ϕ, which would degrade the energy resolution. The readout electrodes, made of copper and kapton, are installed between the lead plates.

The electrodes are separated from the lead by spacer meshes. The remaining space is filled with liquid argon. The argon is cooled by a cryostat system; the barrel part shares the same cryostat vessel with the solenoid magnet. The barrel and end-cap modules are divided into three longitudinal compartments (samplings). The front compartment is finely segmented in $|\eta|$, which makes a good γ/π_0 and e/π separation possible. The middle compartment is the deepest, hence contains most of the shower energy generated by incident electrons or photons. The last compartment is used to complete the energy measurement of showers for higher energies and for estimations of leakage behind the calorimeter. In the following chapter is given a detailed description of the LAr Calorimeter.

The hadronic calorimeter

The hadronic calorimeter [4] is built around the electromagnetic calorimeter. It will measure the energy and direction of jets of particles, formed by the hadronization of quarks and gluons, and by hadronically decaying $\tau-$leptons. The barrel part, called the tile calorimeter, consists of a central barrel ($0 < |\eta| < 1.0$) and two extended barrels ($0.8 < |\eta| < 1.7$). The tile calorimeter uses iron plates as the absorber, which also serve as the return yoke for the solenoid magnet. The active medium is formed by scintillator plastic tiles, which are read out on both sides by optical fibers. The tiles are placed radially, normal to the beam line, and are staggered in depth. Cells are formed by grouping tiles together. The calorimeter has three compartments or samplings in depth read out independently. The readout cells are approximately projective to the interaction point, and have a granularity of $\delta\eta \times \delta\phi = 0.1 \times 0.1$ (0.2×0.1 in the third sampling). The total number of channels is about $10,000$.

The end-cap hadronic calorimeter uses liquid argon technology, because of its higher radiation tolerance. It uses 25 and 50 mm copper plates as the absorber material, arranged in a parallel-plate geometry. The 8.5 mm gaps between the copper plates have three parallel electrodes, thus dividing the gap into four 1.8 mm drift spaces. Smaller drift spaces require a lower voltage (typically 2 kV instead of 4 kV) which reduces the risk of ion build-up and discharge currents. Hadronic showers are much longer than electromagnetic showers, and also much wider. Therefore the hadronic calorimeter needs to be much thicker than the electro-magnetic calorimeter. The total thickness of the calorimeters is more than 10λ, where λ is the interaction length (the mean free path of a hadron between two interactions). This is sufficient to stop almost all the particles that are created in the shower, except muon and neutrinos. However, the calorimeters produce a large background for the muon detector, that consists mainly of thermalized slow neutrons and low-energy photons from the hadronic shower. The Hadronic End-Cap calorimeter is

segmented longitudinally in 4 compartments.

The forward calorimeter

The forward calorimeter (FCAL) is a copper-tungsten calorimeter. It covers the region $3.1 < |\eta| < 4.9$. It is split longitudinally into an electromagnetic compartment, and two hadronic compartments. The copper and tungsten have a regular grid of holes that hold the tube- and rod-shaped electrodes. The space between the tubes and rods is filled with liquid argon. The FCAL is integrated in the same cryostat as the electromagnetic and hadronic end-cap calorimeters.

2.2.3 The muon spectrometer

The muon system [5] is by far the largest subdetector in ATLAS. High$-p_T$ muons are a signature of interesting physics, therefore the muon trigger and reconstruction is very important. The muon system is designed to achieve a momentum resolution of 10% for 1 TeV muons. Fig 2.4 gives an overview of the detector layout.

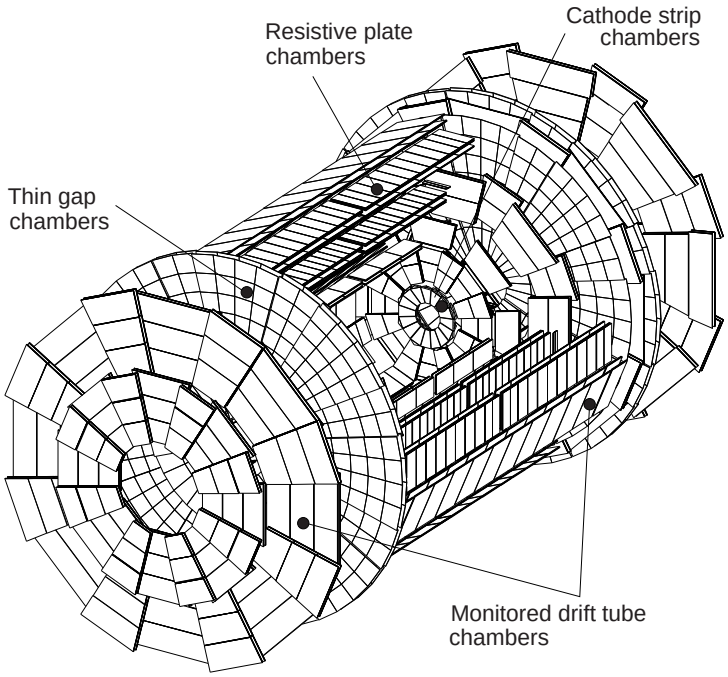

Figure 2.4: *Three-dimensional view of the ATLAS muon spectrometer*

The magnet system in the muon detector is completely independent from the inner

detector. It consists of eight superconducting coils in the barrel, and one eight coils each toroid per end-cap. The magnet is an air-core magnet system, i.e. the space between the coils is left open. Filling this space with iron would enhance the field strength and would also make the field more uniform, but it would also induce multiple scattering that would degrade the momentum resolution. The air-core system has an average field strength of 0.5 T. Four types of detection chambers are used in the muon system: Monitored Drift Tube (MDT) chambers, Resistive Plate Chambers (RPCs), Thin Gap Chambers (TGCs) and Cathode Strip Chambers (CSCs). The MDT chambers provide precise muon tracking and momentum measurement. The chambers consist of aluminium tubes with a 30 mm diameter and a central wire.A muon that crosses a tube will produce ionization clusters in the gas (Ar/CO_2), which will drift to the wire. The distance between the muon and the wire is determined by measuring the drift time of the first cluster that reaches the wire and passes over a threshold. The resolution on the drift distance is around 80 μm. In the inner-most ring of the inner-most end-cap layer, CSCs are used instead of MDT chambers because of their finer granularity and faster operation. They are multiwire proportional chambers. The precision coordinate is read out with cathode strips, the second coordinate is read out using strips which are parallel to the anode wires (orthogonal to the cathode strips). The spatial resolution on the precision coordinate is around 60 μm. The RPCs and TGCs are the muon trigger chambers in ATLAS. Their task is also to identify the bunch crossing to which a trigger belongs. Their adequate position resolution (about 1 cm) and excellent time resolution (about 2 ns) make them well suited for this task. The TGCs are multiwire proportional chambers. The position measurement in these chambers is obtained from the strips and the wires, which are arranged in groups of 4 to 20 wires.

Chapter 3

ATLAS Electromagnetic calorimeter

In this chapter an overview of the main characteristics of the Electromagnetic (EM) Calorimeter is given, specially those relevant to the research work of this document.

3.1 Performance requirements

For electromagnetic calorimetry some of the general requirements to fulfill the physics program are:

- **Rapidity coverage** Searches for rare processes require an excellent coverage in pseudorapidity, as well as the measurement of the missing transverse energy of the event and the reconstruction of jets.

- **Excellent energy resolution** To achieve a 1% mass resolution for the $H \rightarrow \gamma\gamma$ and $H \rightarrow 2e^{+}2e^{-}$ in the range $114 < m_H < 219$ for the standard model Higgs, the sampling term should be at the level of $10\%/\sqrt{E[GeV]}$ and the constant term should be below 0.7%.

- **Electron reconstruction capability from** $1\,GeV$ **to** $5\,TeV$. The lower limit comes from the need of reconstructing electrons from *b* quark decay. The upper one is set by heavy gauge boson decays.

- **Excellent** γ/jet**,** e/jet**,** τ/jet **separation**, which requires again high transverse granularity and longitudinal segmentation.

- **Accurate measurement of the shower position**. The photon direction must be accurately reconstructed for the invariant mass measurement in $H \rightarrow \gamma\gamma$ decay. This

implies a very good transverse and longitudinal segmentation, with a measurement of the shower direction in θ with an angular resolution of $\sim \frac{50mrad}{\sqrt{E(GeV)}}$.

- **Small impact of Noise** The impact of noise on the calorimeter performance must be as small as possible. At LHC, contributions to the calorimeter resolution from noise arise from pile-up and from the electronic noise of the readout chain. These contributions are particularly important at low energy ($E < 20\ GeV$) where they can dominate the accuracy of the calorimeter energy and position measurements. Minimization of the pile-up noise requires fast detector response and fast electronics; minimization of the electronic noise requires high calorimeter granularity and high-performance electronics.

- **Resistance to radiation** The EM calorimeters will have to withstand neutron fluencies of up to $10^{15}\ \frac{n}{cm^2}$ and radiation doses of up to 200 kGy (integrated over ten years of operation).

- **Time resolution** The time resolution should be around 100 ps for background rejection and for the identification of some decay modes with non-pointing photons.

- **Linearity** It is necessary to obtain a linearity better than 0.1%.

In order to fulfill these requirements precise optimal filtering coefficients (OFC) must be determined, which imply an accurate knowledge of the pulse shape response of every calorimeter channel. This will be discussed in next chapters.

3.2 Generalities of the EM calorimeter

The electromagnetic (EM) calorimeter is a sampling calorimeter with lead as absorber or passive material and Liquid ARgon (LAR) as an active material [16]. An accordion shape is given to all plates in order to avoid crack regions due to cables and boards of the readout. For the sake of clarity a photograph of the accordion shape corresponding to the EMEC inner wheel can be seen in figure 3.1. Particles would be incident from left to right on the figure.

The LAR ionization is collected by electrodes (at high voltage) situated in between two absorbers (at ground); see Figure 3.2. To keep the electrode in the right place, honeycomb spacers are located in between the absorber and the electrode. Hence, the calorimeter is stacked as a sandwich of absorber, spacer, electrode, spacer, (next absorber), repeated along the azimuthal direction up to complete the whole coverage.

The EM Calorimeter covers the whole range along the azimuthal (ϕ) direction and between -3.2 and 3.2 along the η direction. It is divided in one barrel ($-1.475 < \eta <$

Figure 3.1: Accordion shape in EMEC inner wheel

Figure 3.2: Stacked layer. The electrode is placed in between two absorbers.

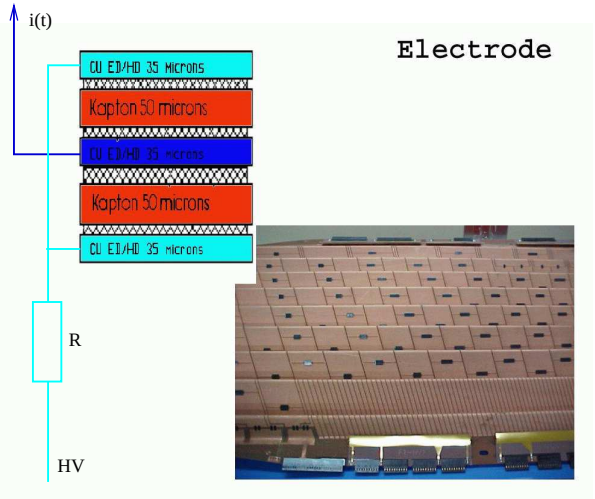

Figure 3.3: Picture of an EMEC electrode. The thin electrode has 3 layers separated by Kapton isolation: two HV layers on the sides and one signal layer inbetween which capture the ionization signal by capacitance coupling..

1.475) [17] and two end-caps ($-3.2 < \eta < -1.375$, $1.375 < \eta < 3.2$) [18] and is segmented in depth in three compartments (see figure 3.5). There is also a thin presampler detector in front of the calorimeter covering the region $|\eta| < 1.8$, which task is to correct for the energy losses of electrons and photons in the upstream material.

The Argon is kept liquid at a temperature of $\sim 89^{o}K$ through a cryogenic system, being the EM barrel and end-cap calorimeters inside their respective cryostat vessels.

3.3 End-cap specifities

There are two EMEC cylinders in ATLAS located inside the End-cap Cryostat at $z \sim \pm 350$ cm of the nominal interaction point. A picture of one EMEC inside the End-Cap cryostat can be seen in figure 3.4. Since the EMEC is a cylindrical wheel, the amplitude of the accordion waves decreases when η increases (when the radious decreases). Due to mechanical constraints demanded by this accordion shape, a second independent wheel is needed to extend the coverage to $\eta = 3.2$. Hence, there are two wheels, the outer wheel from $\eta = 1.375$ to $\eta = 2.5$ and the inner wheel from $\eta = 2.5$ to $\eta = 3.2$. The lead is cladded by 0.2 mm thick steel to give it enough rigidity. For the outer wheel, the thickness of the lead plates is 1.7 mm while the LAR gap thickness between the absorber and the electrode decreases continuously from 2.8 mm (at $\eta = 1.375$) to 0.9 mm (at $\eta = 2.5$) when η increases. For the inner wheel, the thickness of the lead plates is 2.2 mm while

the LAR gap thickness between the absorber and the electrode decreases continuously from 3.1 mm (at $\eta = 2.5$) to 1.8 mm (at $\eta = 3.2$) when η increases.

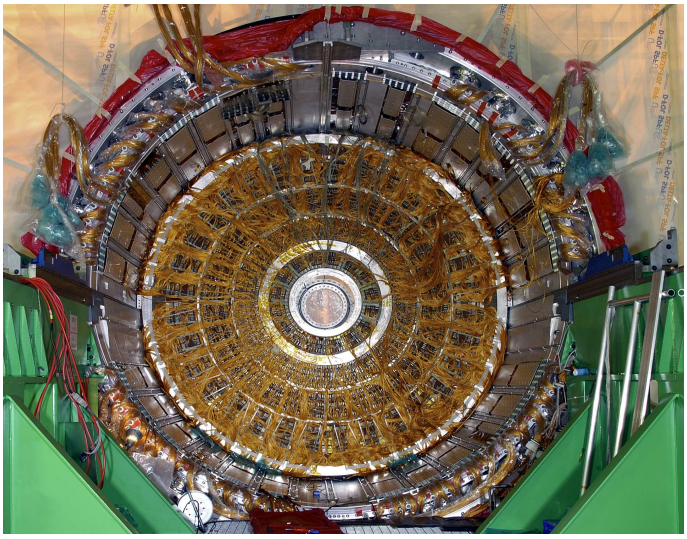

Figure 3.4: Picture of an EMEC wheel inside the End-Cap Cryostat.

To facilitate handling and logistics the EMEC cylinder is divided into 8 octants or modules (see figure 3.6). The 16 modules have been stacked in the CPPM [1] and UAM [2] clean rooms.

One module consists of 96 (32) layers for the outer (inner) wheel stacked one on top of each other. Each layer is a sandwich of absorber, spacer (gap), electrode, spacer (gap). The design is symmetrical in ϕ and projective to the interaction point in η. In particular the cells drawn in the electrodes point to the nominal ATLAS interaction point.

[1] Centre de Physique des Particules de Marseille
[2] Universidad Autónoma de Madrid

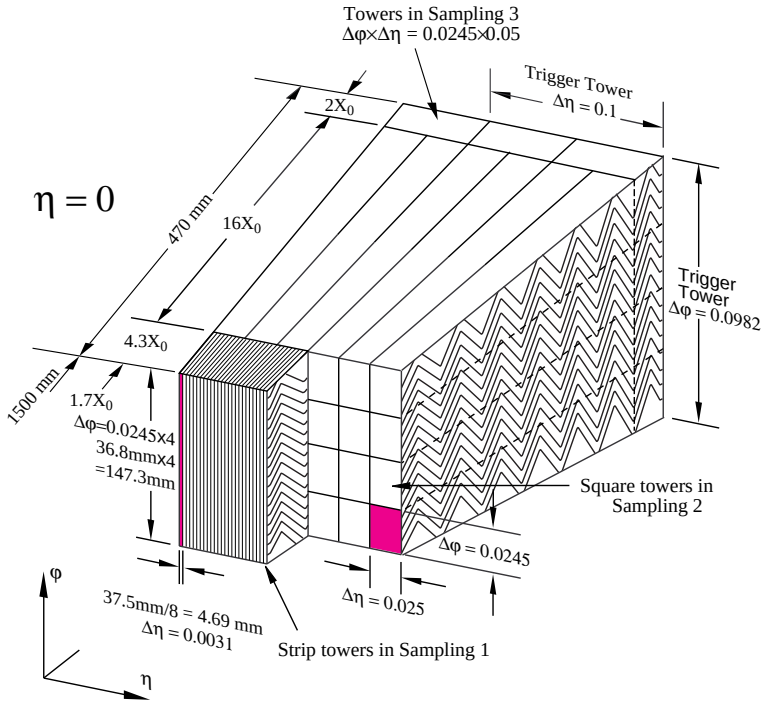

Figure 3.5: *Schematic view of an accordion calorimeter piece. A representation of the 3 compartments in depth is shown as well as some dimensions.*

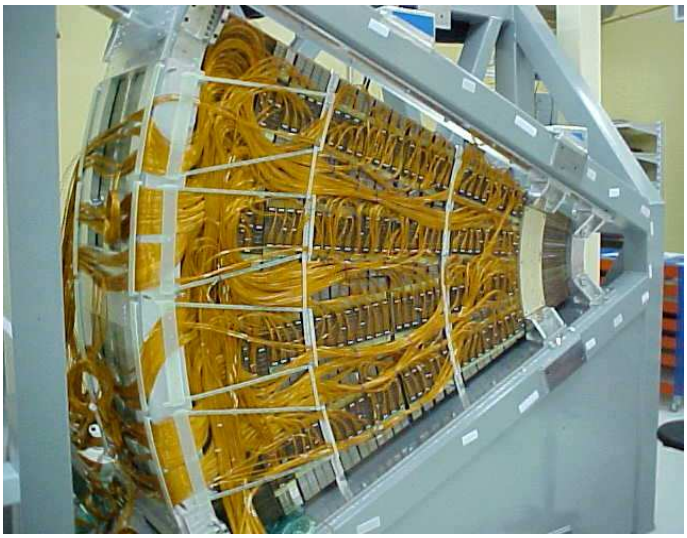

Figure 3.6: Picture of an EMEC module or octant at the stacking frame of the UAM clean room.

3.4 Barrel specifities

The barrel electromagnetic calorimeter (EMB) is made of two half-barrels, centered around the z-axis. One half-barrel covers the region $0 < \eta < 1.475$ and the other one the region $-1.475 < \eta < 0$. The length of each half-barrel is 3.2 m, their inner and outer diameters are 2.8 m and 4 m respectively.

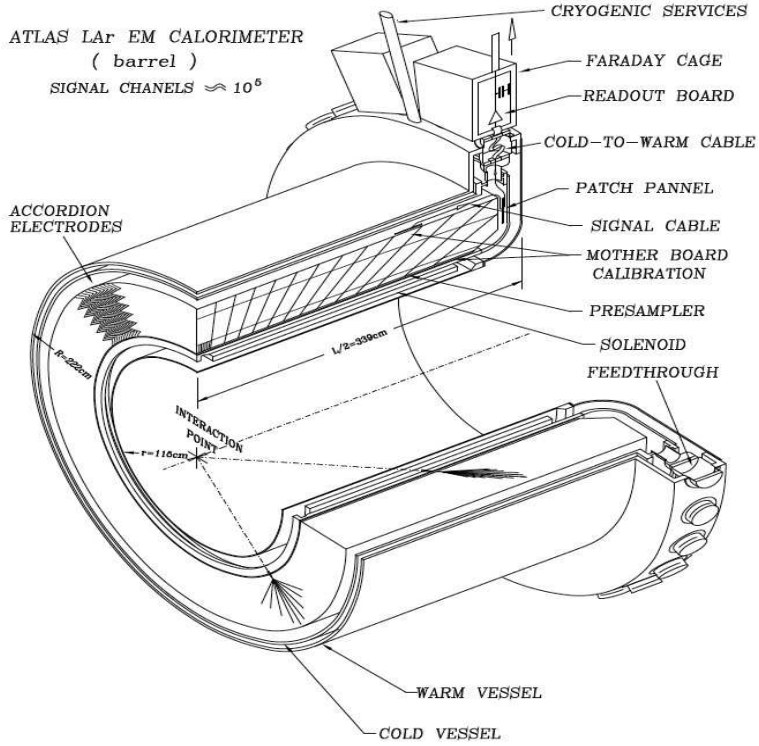

Figure 3.7: Diagram of a half of the EM Barrel.

Figure 3.7 shows a diagram of one half-barrel. The direction of the accordion waves is indicated pointing to the *z* axis as well as the calorimeter cells which points to the ATLAS center or nominal interaction point. The calorimeter is inside the cryostat vessel which has two walls, warm and cold, separated with a vacuum gap for temperature isolation purposes. The cables pass from inside to outside of the cryostat vessel using special feedthrough connectors which keeps the temperature isolation. In the ”warm” part (outside the cryostat) crates are connected to the feedthroughs, which contains some electronics boards: Front End Boards (FEB) and Calibration Boards. It can also be seen in figure 3.7 a tube on top of the cryostat through which the cryogenic system injects the liquid Argon.

The size of the LAR gap on each side of the electrode is 2.1 mm, which corresponds

to a total drift time of about 450 ns for an operation voltage of 2000 V. For ease of construction, each half-barrel has been divided into 16 modules, each covering a $\Delta\phi = 22.5^o$. A picture of one EMB module is shown in figure 3.8.

Figure 3.8: Picture of an EMB module.

3.5 Segmentation

The EM Calorimeter is segmented into cells along the two angular directions, η and ϕ, and the longitudinal direction (calorimeter depth). Along the calorimeter depth three compartments are defined, by reading out three regions of the electrode independently, namely: Front or S1, readout from the calorimeter front side, Middle or S2 and Back or S3, both readout from the calorimeter back side (see figure 3.5).

The granularity along η is also defined in the electrodes as copper strips using kapton as electrical isolator between two strips. The size of such strips depends on the compartment, being smallest in the S1 to allow for the separation of the two photons from the decay of a π^0. A picture of an EMEC electrode (outer wheel) is shown in figure 3.9. The angular variable η increases from right to left of the picture. The copper strips are clearly seen defining the granularity along the η direction. The three compartments in depth, S1, S2 and S3, can be clearly distinguished as the width of the strips changes from one compartment to another.

The granularity along the azimuthal ϕ direction is defined by connecting summing boards to the electrode connectors, hence grouping the signal in ϕ. For example, for the S2 compartment of the EMEC, three consecutive electrodes are connected (are summed)

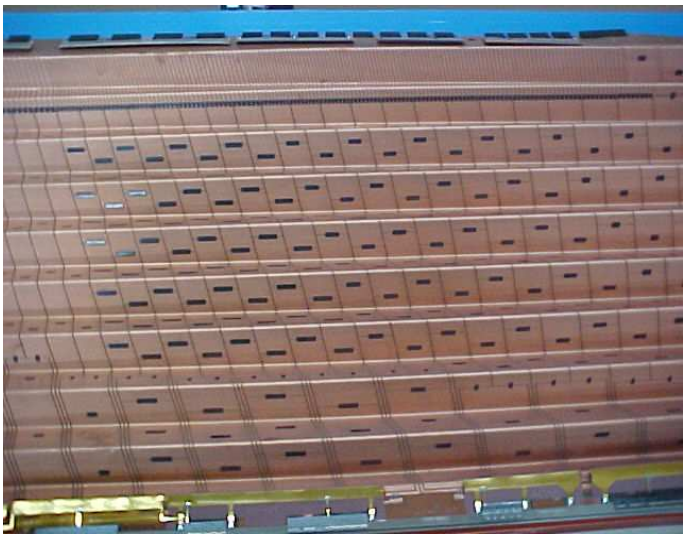

Figure 3.9: Picture of an EMEC electrode of the outer wheel. The segmentation along η and the three compartments in depth, S1,S2 and S3, are clearly seen.

to obtain the desired granularity of $\Delta\phi = 0.025$ radians, while 12 electrodes are connected for the S1 compartment of the EMEC given a granularity of $\Delta\phi = 0.1$ radians in this compartment. Figure 3.10 shows some summing boards plugged in the electrode connectors for the S1 compartment of an EMEC module. The ϕ direction goes from bottom to top of the picture, while the η direction increases from left to right. The electrode connectors can be distinguished in black between two absorbers. The summing boards grouped the signals of 12 electrodes together in this example.

The electromagnetic calorimeter granularity is detailed in Table 3.1. In total the number of cells or channels in the electromagnetic calorimeter is $\sim$ 170000 (101 760 in barrel, 62 208 in end-caps and 9 344 in presampler).

3.6 High Voltage

The High Voltage (HV) between the electrodes and absorbers is generated by some special HV units outside the cryostat. The HV thin cables pass through some dedicated cryostat feedthroughs to reach the HV boards on the calorimeter. A picture of one EMEC HV board is shown in figure 3.11. It is plugged into some dedicated connectors of the electrodes. The ϕ direction goes from left to right and η increases from top to bottom in the figure. There is one column of HV boards along ϕ-direction per high voltage value (per high voltage region).

The condition of projectivity to the nominal ATLAS interaction point in the con-

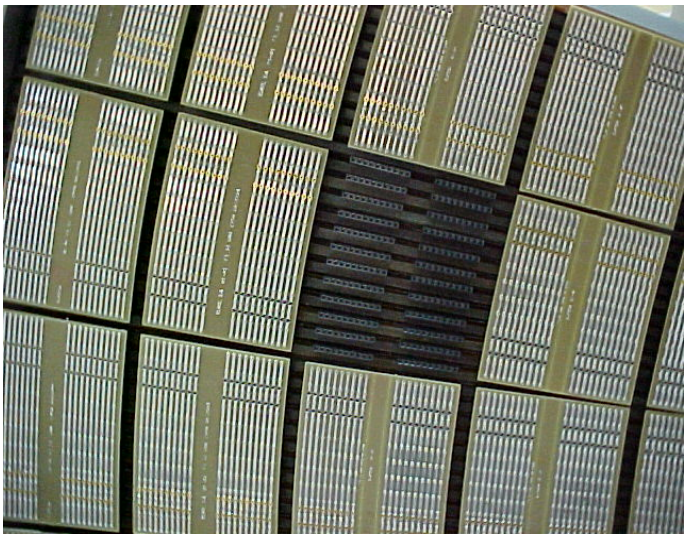

Figure 3.10: Picture the summing boards plugged in the front face of an EMEC module.

		Front (S1)	Middle (S2)	Back (S3)
Barrel	$\|\eta\| \leq 1.35$	$0.025/8 \times 0.1$	0.025×0.025	0.050×0.025
	$1.35 \leq \|\eta\| \leq 1.4$	$0.025/8 \times 0.1$	0.025×0.025	–
	$1.4 \leq \|\eta\| \leq 1.475$	0.025×0.025	0.075×0.025	–
End-caps	$1.375 \leq \|\eta\| \leq 1.425$	0.050×0.1	0.050×0.025	–
	$1.425 \leq \|\eta\| \leq 1.5$	0.025×0.1	0.025×0.025	–
	$1.5 \leq \|\eta\| \leq 1.8$	$0.025/8 \times 0.1$	0.025×0.025	0.050×0.025
	$1.8 \leq \|\eta\| \leq 2.0$	$0.025/6 \times 0.1$	0.025×0.025	0.050×0.025
	$2.0 \leq \|\eta\| \leq 2.4$	$0.025/4 \times 0.1$	0.025×0.025	0.050×0.025
	$2.4 \leq \|\eta\| \leq 2.5$	0.025×0.1	0.025×0.025	0.050×0.025
	$2.5 \leq \|\eta\| \leq 3.2$	0.1×0.1	0.1×0.1	–

Table 3.1: *Granularity $\Delta\eta \times \Delta\phi$ for each calorimeter sampling (Front, Middle and Back).*

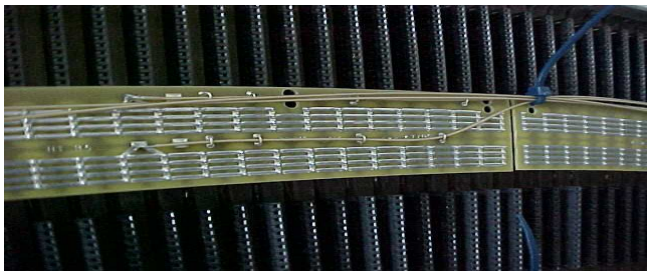

Figure 3.11: Picture of an EMEC HV board

struction of the EMEC makes that the Liquid Argon gap thickness (between absorber and electrode) decreases continuously when η increases. The relation between the energy collected by the calorimeter (E) and the liquid Argon gap thickness (g) is [6]:

$$E \sim \frac{f_s}{g^{1+b}} U^b \tag{3.1}$$

where U is the High Voltage applied on the gaps and f_s the sampling fraction [3] (which is a function of the gap thickness).

The decrease of the liquid Argon gap thickness when η increases implies an increase of the measured energy with η. This growth may be compensated by decreasing U continuously when η increases. For practical reasons a decreasing stepwise function for U is chosen defining seven HV sectors for the outer wheel and two sectors for the inner wheel. The growth of the measured energy with η inside a HV sector is corrected by software in the reconstruction phase of the signal, keeping then the required uniformity of the calorimeter signal response.

In contrast, for the EM Barrel Calorimeter this problem does not occur and, as a consequence, the High Voltage between electrodes and absorbers is kept constant, being the nominal value 2000 Volts.

The High-Voltage sector definitions, consequence of the end-cap geometry, is given in Table 3.2.

[3] The sampling fraction is defined as the energy deposited in the LAR divided by the sum of the energy deposited in the Absorbers and the LAR.

	Barrel	End-cap Outer W.							End-cap Inner W.	
HV region	0	1	2	3	4	5	6	7	8	9
η range	0-1.475	1.375-1.5	1.5-1.6	1.6-1.8	1.8-2.0	2.0-2.1	2.1-2.3	2.3-2.5	2.5-2.8	2.8-3.2
HV values	2000 V	2500 V	2300 V	2100 V	1700 V	1500 V	1250 V	1000 V	2300 V	1800 V

Table 3.2: *The high voltage regions of the EM calorimeter.*

3.7 Electronics

The electric signal from the ionization of the Liquid Argon produced by a charged particle has a triangular shape, when representing the intensity versus time, with typical duration of several hundreds nano-seconds. This signal pass through the electrode readout paths to the Summing Boards and the Mother Boards on top of them. Long cables connect the Mother Boards to the electronics outside the cryostat. A picture of the Summing Boards can be seen in figure 3.10 and of the Mother Boards in figure 3.12.

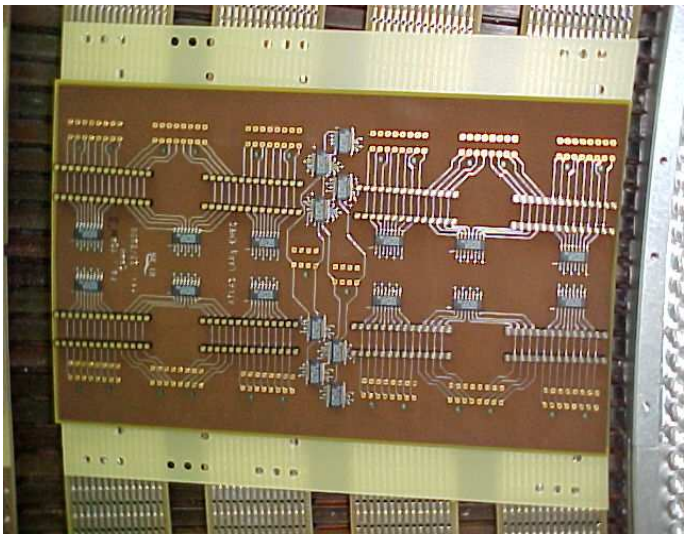

Figure 3.12: Picture of one Mother Board of the front side of the EMEC.

A simplified schematic view of the calorimeter readout is shown in figure 3.13. The detector cell is represented by a capacitance C where a triangular ionization signal ($I_{inj}^{phys}(t)$) is generated by the detected particle. Also linked to a cell there appears an inductance L due to the electrode, the Summing-Board and a small portion of the Mother-Board. The signal travels through a 25Ω cable in case of a middle or a back cell and a 50Ω cable in case of a front cell. Immediately after the feedthrough of the cryostat the signal enters a Front-End-Board (FEB) and pass through a three gain shaper with gain factors 1, 9.3 and 93 corresponding to low, medium and high gain respectively. The measured

shaped signal $g^{phys}(t)$ is sampled by a Switch Capacitor Array (SCA) located in the FEB at a frequency of 40 MHz (equivalent to a period of 25 ns), that is the nominal bunch crossing frequency of LHC beams. The samples are digitized by ADCs located in the FEB and the numbers are transmitted to the miniROD and the DAQ computing system in the control room (see figure 3.14).

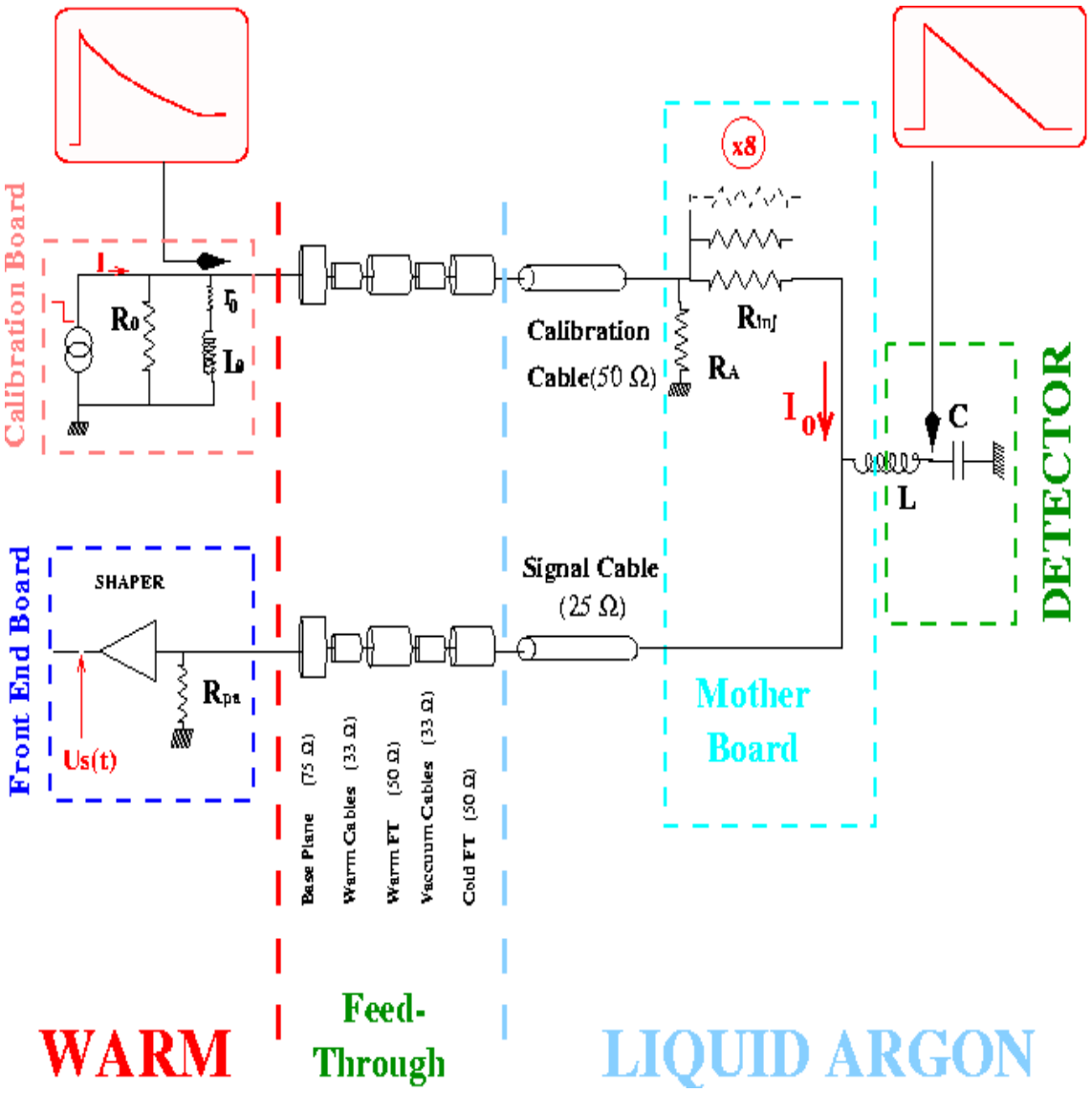

Figure 3.13: Diagram of the EM calorimeter readout inside the detector.

A diagram of one calibration line is also shown in figure 3.13. An exponential signal ($I_{inj}^{cali}(t)$) is generated in the Calibration Board playing the role of the triangular ionization signal (I_p) of physics events. The signal I_{inj}^{cali} pass the feedthrough to get into the cryostat

and travels through a long cable up to the Mother-Board. The calibration signal sees the detector cell as a capacitance and an inductance as indicated in figure 3.13. The response to this injection signal continues through the same readout line as the ionization signal to reach the SCA. The output is again seven samples of the shaped signal $g^{cali}(t)$ after being digitized by the ADC.

The calibration boards allow to set the amplitude of injected current I_{inj}^{cali} numerically. A DAC unit, included in the calibration board, transforms this number into an analog amplitude. We will refer to this number as DAC value. The calibration board is equipped with a delay unit, which allows to delay the injection from 0 to 24 ns in steps of 1 ns with respect to the leading edge of the 40 MHz clock (t_{delay}). The calibration pulse $g^{cali}(t)$ is obtained by representing the sample heights as a function of t_{delay}. [4]. These delay runs were taken inbetween cosmic runs. Delay runs in high (medium, low) gain with a DAC value of 500 (4000,40000) units are considered for the signal reconstruction studies.

3.8 Some differences between EMEC and EMB

Some differences between EMEC and EMB relevant to the study of this document are summarized in table 3.3.

	Barrel	End-caps (outer wheel)
Gap (absorber-electrode) (mm)	2.1	3.1 to 0.9
Bending angle ($^\circ$)	70 to 90	60 to 120
Drift time (ns)	470	600 to 200
dE/dX sampling fraction (%)	25 or 28	30 to 14
HV (V)	2000	2500 to 1000
S2 Cell inductance L (nH)	25 to 35	50 to 20
S2 Cell Capacitance at cold C (pF)	1400 or 1900	1200 to 600

Table 3.3: *Some geometrical and electrical characteristics of the barrel and end-cap outer wheel EM calorimeter. In the former case, parameters may vary at* $|\eta| = 0.8$. *In the latter case, the variation is smooth and given for increasing* $|\eta|$ *from 0 to 2.5.*

[4] Every sample height is an average over 100 events taken for a given delay

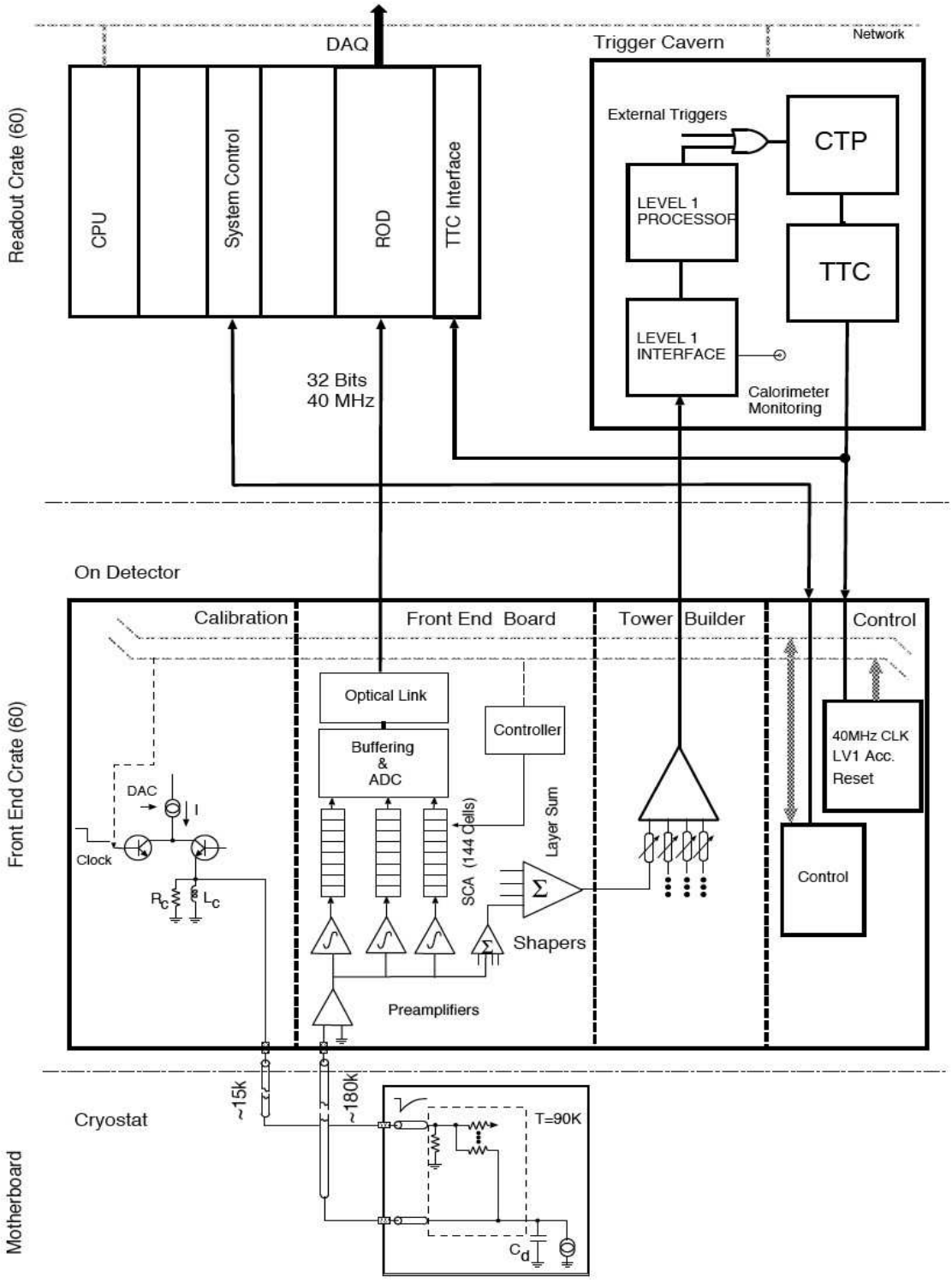

Figure 3.14: Diagram of the EM calorimeter readout

Chapter 4

Signal Reconstruction Algorithms

The ATLAS Liquid Argon electromagnetic calorimeter uses a digital filtering technique, called Optimal Filtering Method, to reconstruct the signal amplitude from samplings of the ionization pulse. Some weights, optimal filtering coefficients, are determined from the pulse shape and its derivative, such that the weighting sum of the samplings gives the amplitude of the signal per cell. Each read-out channel can be calibrated by means of electronic pulses that mimic the ionization signal produced by an electromagnetic shower. The calibration and the ionization signal are different in shape (exponential/triangular, respectively) and injection point (outside/inside the detector). It is necessary to know the electrical parameters of every cell in the detector to deduce the ionization signal using the calibration signal.

This chapter gives a brief description of the Optimal Filtering Method, the detector model, the prediction of the ionization signal from the calibration signal and an algorithm to determine the electrical parameters of the calorimeter cell.

4.1 Optimal filtering method

The LAr EMC signal is generated by the drift of the ionization electrons in the electric field provided by the High Voltage (HV) in the LAr gap. The current versus time has a triangular shape, being the peak proportional to the energy deposited by the electromagnetic shower. The ionization signal is pre-amplified and then shaped by a $CR-RC^2$ bipolar filter at the end of the readout chain. The bipolar signal is sampled every 25 ns (the LHC bunch crossing period) and 5 samples are digitized and used in the signal reconstruction procedure. For special runs more than 5 samples are digitized and recorded (typically 25 or 32). Figure 4.1 shows a comparison between the original triangular signal generated inside the LAr gap and the output signal after passing the readout electronics.

It corresponds to a cell of the S_2 compartment for medium gain of the bipolar shaper. The maximum has been normalized to 1. The bipolar shaper is designed such that the maximum of the triangular signal corresponds to the maximum of the shaped pulse. Hence, the maximum amplitude of the shaped pulse is proportional to the energy deposited by the electromagnetic shower in that S_2 cell. The dots correspond to the samples each 25*ns*.

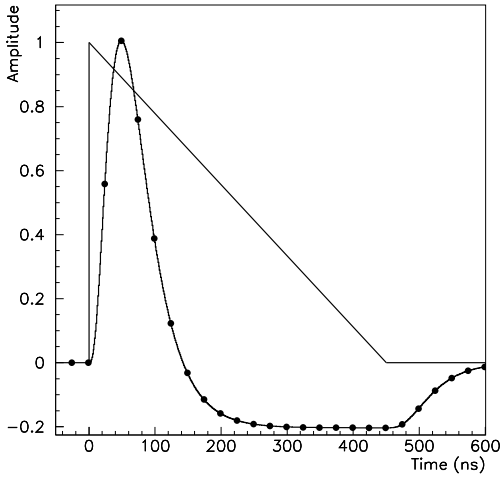

Figure 4.1: The triangle shape corresponds to the signal as a function of time just after the electrode, and the bell shape corresponds to the signal after crossing the shaper. Dots represent the recorded amplitudes separated by 25 ns.

From these samples two relevant quantities are deduced, using a digital filtering technique, namely the signal maximum amplitude (A_{max}), which is proportional to the energy deposited in the cell, and the time shift (Δt) of the signal maximum amplitude with respect to a reference value. The Optimal Filtering (OF) method is a digital filtering technique to determine such quantities. The inputs to the method are: i) the covariance or autocorrelation matrix of the samples, which contains the information of the noise, ii) the pulse shape (g^{phys}), its maximum normalized to one, ii) and its derivative (dg^{phys}/dt). The outputs of the method are some weights or coefficients, $a_i,\ b_i\ \ i = 1,\ldots,n$, where n is the number of samples, such that:

$$A_{max} = \sum_{i=1}^{n} a_i S_i \tag{4.1}$$

$$\Delta t = \frac{\sum_{i=1}^{n} b_i S_i}{A_{max}} \tag{4.2}$$

being $S_i\ i = 1,\ldots,n$ the measured samples (pedestal or zero is subtracted).

The Optimal Filtering coefficients (OFC), $a_i,\ b_i\ \ i = 1,\ldots,n$, are calculated by the method with the condition to minimize the noise contribution to the signal [19].

Two sources of noise are foreseen in the calorimeter during operation at LHC:

- Thermal (or electronic) noise

  The amplitude of the thermal noise depends only upon the characteristics of the detector and the signal processing circuitry.

- Pile-up (or physics) noise

  The minimum bias or soft scattering events will be superimposed to the hard scattering process. It is expected to have about 27 minimum bias events per bunch crossing at nominal LHC luminosity. In addition, events of previous bunch crossings will affect the signal of the present crossing, since the ionization time constant of the liquid Argon is several hundred nano-seconds. The overall effect is a small signal in the cells, fluctuating from event to event, which can be considered as a noise superimposed to the hard process physics event of interest. The level of pileup noise depends therefore on the luminosity of the machine and on the size of the calorimeter cells.

Since the present work refers to cosmics muon data, only the first source of noise enters in the analysis. In future, for the analysis of the LHC data we will need to take the pile-up noise contribution into account as well.

In ATLAS, where the bunch crossings and the readout clock are synchronous the pulses get always sampled at the same position and one set of OFC is sufficient. However, in the cosmic test environment this is not the case since the cosmic signal is asynchronous to the readout clock. Depending on the phase shift between the clock and the particle arrival, a different fraction of the pulse is sampled. To cope with this situation, multiple sets of OF coefficients are calculated dividing the 25ns region between two ADC samples in bins of $\Delta t \backsim 1\ ns$. For the present analysis, a set of $(a_i, b_i), i = 1,\ldots,n$ coefficients for each time phase has been calculated, up to a total of 50 phases in 1ns steps and for high gain. Medium and low gains are not used since most of the muons deposit an energy lower than 20 GeV in the EM Calorimeter. The fact of duplicating the number of phases in the analysis, 50 instead of 25, allows to perform cross-checks at different timings and guarantees to cover completely the 25ns region of interest.

4.1.1 Prediction of physics pulse

As seen in the previous section, the pulse shape of the ionization (or physics) signal is needed to determine the Optimal Filtering Coefficients for each calorimeter cell. However

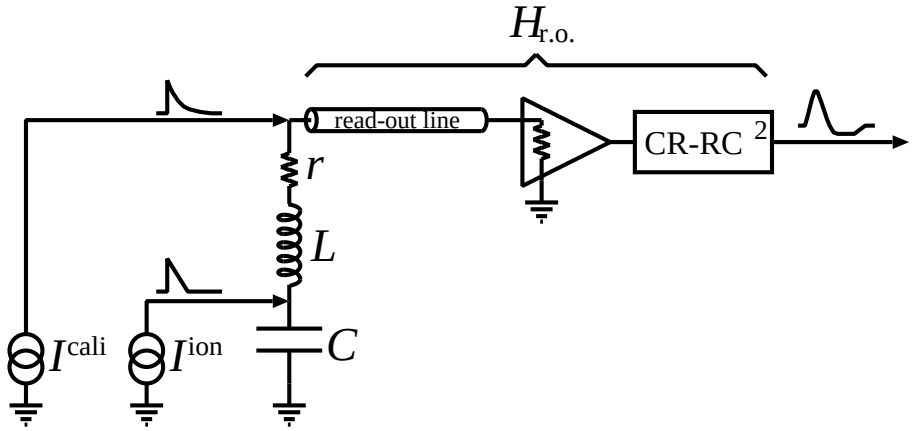

Figure 4.2: *Schematic electrical model of a LAr cell with its readout chain and calibration network. Shapes of calibration and ionization signals are illustrated, as well as the output pulse.*

this shape is unknown and must be predicted either by a complete description of the readout chain or from the corresponding calibration pulse shape and a few parameters (due to the differences between the ionization signal and the calibration signal). The second procedure has been adopted in this work.

Although the readout path and electronics is the same for physics and calibration inputs, there are two differences at the injection point, namely:

- the physics input signal is produced inside a gap of the detector, while the calibration input is generated outside the cryostat in a calibration board connected on a Front End Crate. This difference makes the calibration see the calorimeter cell as a different *rLC* circuit.

- the physics input signal has a triangular shape when represented as a function of time, while the calibration charge injection has an exponential shape.

In figure 4.2 a simplified diagram of the electrical model for a LAr cell is shown. The calorimeter cell is seen as an *rLC* circuit: the capacitance *C* of the LAr gap, an inductance *L* which has two contributions, one from the electrode path between the gap and the Summing Board and the other one from the path inside the Summing Board itself added to a small portion of Mother Board, and a small resistance *r* of the total path. The injection point of the ionization (physics) and calibration signals is indicated as well. Clearly these signals see the cell *rLC* circuit in a different way, *rL* in parallel with *C* for physics injection signal and in serial in the case of calibration. The different shapes of the injection current between physics and calibration (triangular and exponential) is also shown.

The ionization electrons drift in the electric field inside the LAr gap, producing a current with amplitude proportional to the released energy. This current has the typical ionization-chamber triangular shape, with a rise time of the order of 1 ns followed by a linear decay for the duration of the maximum drift time t_{drift}. Such a signal at the input of the cell capacitor in time domain is given by:

$$I_{inj}^{phys}(t) = I_0^{phys}\theta(t)\theta(t_{drift}-t)(1-\frac{t}{t_{drift}}) \tag{4.3}$$

where θ is the *Heavyside* function and I_0^{phys} is the amplitude of the ionization current. The drift time t_{drift} in a 2 mm gap under a voltage of 2000 V is close to 400 ns. This time is a function of the pseudorapidity for the EMEC due to the change in the LAr gap and in the voltage, taking values in the range 200-600 ns.

The output physics signal can be written as:

$$g^{phys}(t) = \int_{-\infty}^{+\infty} K_p(t-t')I_{inj}^{phys}(t')dt'$$

where K_p contains the information of the readout circuitry.

In the Laplace domain (applying the "Convolution Theorem"), we find:

$$g^{phys}(s) = I_{inj}^{phys}(s)K_p(s)$$

where:

- $K_p(s)$ can be written as the product of a factor $H^{det}(s)$, which contains the electronics characteristics related to a detector cell (*rLC* circuit), and a factor $H^{readout}(s)$, which takes into account the readout chain (common for physics and calibration signals);
- $I_{inj}^{phys}(s)$ is the injected ionization signal 4.3 in the Laplace frequency domain, that is:

$$I_{inj}^{phys}(s) = I_0^{phys}(\frac{1}{t_{drift}s} - \frac{1-e^{-t_{drift}s}}{t_{drift}^2 s^2})$$

Hence, the output physics signal can be written as:

$$g^{phys}(s) = I_{inj}^{phys}(s)H^{det}(s)H^{readout}(s)$$

The calibration charge injection aims to mimic the ionization signal, in order to be able to measure the actual gain and properties of each channel thus assuring the proper cell equalization. An exponential signal with decay time τ_{cali} is generated by the calibration boards (see section 3.7), whose pulser is based on a RL-circuit (see figure 3.13). The values of the R_0 and L_0 components are selected such that to obtain the proper exponential decay constant τ_{cali}, which has been chosen similar to the ionization signal decay slope. The non-ideal inductance L_0 of the calibration board pulser circuit has a resistive component r_0 that modifies the baseline of the exponential (f_{step} parameter below). This exponential injection current can be written as:

$$I_{inj}^{cali}(t) = I_0^{cali}\theta(t)(f_{step} + (1 - f_{step})e^{-t/\tau_{cali}}) \tag{4.4}$$

where I_0^{cali} is the amplitude of the injected current, $\theta(t)$ is the *Heavyside* step function, f_{step} (between 0 and 1) is the fraction

$$f_{step} = \frac{r_0}{r_0 + \frac{R_0}{2}}$$

and τ_{cali} is the effective exponential decay constant (which value is approximately 360 ns)

$$\tau_{cali} = \frac{L_0}{r_0 + \frac{R_0}{2}}$$

Similarly to the the ionization physics signal, the calibration signal at the output of the readout chain can be written in the Laplace frequency domain as:

$$g^{cali}(s) = I_{inj}^{cali}(s)H^{detcali}(s)H^{readout}(s)$$

where

- $H^{detcali}(s)$ is the detector part of the electronics circuit as seen by the calibration injection signal;
- $I_{inj}^{cali}(s)$ is the Laplace transform of the calibration injection signal 4.4, namely:

$$I_{inj}^{cali}(s) = I_0^{cali}(\frac{\tau_{cali}(1 - f_{step})}{1 + \tau_{cali}s} + \frac{f_{step}}{s})$$

Dividing $g^{phys}(s)$ and $g^{cali}(s)$ the common part $H^{readout}(s)$ cancels out and we obtain:

$$\frac{g^{phys}(s)}{g^{cali}(s)} = \frac{I_0^{phys}}{I_0^{cali}} \frac{H^{det}(s)}{H^{detcali}(s)}$$

Hence, the physics signal or physics pulse shape can be obtain from the calibration pulse shape through the following expression in the Laplace frequency domain:

$$g^{phys}(s) = g^{cali}(s) \frac{I_{inj}^{phys}(s)}{I_{inj}^{cali}(s)} \frac{H^{det}(s)}{H^{detcali}(s)}$$

Or in the time domain as:

$$g^{phys}(t) = \left[g^{cali} \times \mathcal{L}^{-1} \left(\frac{I_{inj}^{phys}(s)}{I_{inj}^{cali}(s)} \right) \times \mathcal{L}^{-1} \left(\frac{H^{det}(s)}{H^{detcali}(s)} \right) \right](t) \tag{4.5}$$

where $\times$ means convolution.

The second and third factors in the convolution take into account the differences in the injection signal and injection point respectively between the physics and the calibration signals.

4.2 Computation of g^{phys}

For computational purposes the relation 4.5 can be written as:

$$\begin{aligned} g^{phys}(t) &= \left[g^{cali} \times \mathcal{L}^{-1} \left(\frac{(1+s\tau_{cali})(st_{drift} - 1 + e^{-st_{drift}})}{st_{drift}(f_{step} + s\tau_{cali})} \right) \times \mathcal{L}^{-1} \left(\frac{1}{1+s^2LC+srC} \right) \right](t) \\ &= \left[g^{cali} \times g^{exp \to tri} \times g^{MB \to det} \right](t) \end{aligned} \tag{4.6}$$

where the two different time-domain convolutions are:

$$\begin{aligned} g^{exp \to tri}(t) = \delta(t) &+ \left[\frac{1 - f_{step}}{\tau_{cali}} e^{-f_{step} \frac{t}{\tau_{cali}}} - \frac{1 - f_{step}}{f_{step}} \left(e^{-f_{step} \frac{t}{\tau_{cali}}} - 1 \right) \right] \theta(t) \\ &+ \frac{1 - f_{step}}{f_{step}} \left(e^{-f_{step} \frac{t - t_{drift}}{\tau_{cali}}} \right) \theta(t - T_d) \end{aligned}$$

$$g^{MB\to det}(t) = \frac{2}{\tau_a} e^{(\tau_r/(2\tau_0^2))t}\theta(t)$$

where $\tau_r = rC$ and $\tau_0 = LC$.

The procedure requires the knowledge of the calibration pulse g^{cali} (see chapters 3 and 7) and of a set of five parameters, namely two related to the calibration board, τ_{cali} and f_{step}, two related to the cell electrical properties, τ_0 and τ_r, and one related to the ionization, t_{drift}. Their values may depend on the detector conditions, temperature, radiation dose, etc, hence it is important to monitor them on a regular basis. The parameter t_{drift} has been measured at the beam tests, while the other four parameters can be extracted either from direct measurements or from the calibration pulse using the algorithm called Response Transformation Method (RTM)

4.3 Parameter extraction algorithm (RTM)

The RTM method was developed by the Milan Atlas group to be applied to the Barrel EM calorimeter [11]. The method consists in the following. We have seen that the response to a calibration injection pulse can be expressed in the Laplace frequency domain as:

$$g^{cali}(s) = I_{inj}^{cali}(s) H^{detcali}(s) H^{readout}(s)$$

The function $H^{detcali}(s)$ describes the effects of the detector cell properties on the injected calibration signal $I_{inj}^{cali}(s)$, while $H^{readout}(s)$ is the readout (line+preamplifier+shaper) transfer function.

Let a generic current pulse $Y_{inj}(s)$ be injected on the system at the Mother Board level, as it is actually done with the real calibration pulse $I_{inj}^{cali}(s)$. The response $W_{out}(s)$ of the system to this signal would be:

$$W_{out}(s) = Y_{inj}(s)\, H^{detcali}(s)\, H^{readout}(s) = \frac{Y_{inj}(s)}{I_{inj}^{cali}(s)}\, I_{inj}^{cali}(s)\, H^{detcali}(s)\, H^{readout}(s) =$$
$$= \frac{Y_{inj}(s)}{I_{inj}^{cali}(s)}\, g^{cali}(s)$$

or, in the time domain:

$$W_{out}(t) = \left[g^{cali} \times \mathcal{L}^{-1}\left(\frac{Y_{inj}(s)}{I_{inj}^{cali}(s)} \right) \right](t)$$

The dependence on the circuit parameters has cancels out and only remains the ratio between the different injection functions.

The RTM bases its strategy to retrieve parameters on the computation and analysis of what would be the response to a signal different from the ”exponential” calibration injection signal. The system response can in fact be sensitive to a particular injected waveform, the output showing in some cases easily recognizable characteristics. In the following steps, waveforms will be sought that minimize the signal tail of $W_{out}(t)$. For this purpose, a χ^2-like quantity is built by summing the squares of the values of $W_{out}(t)$ along the tail, that is:

$$Q^2 = \sum_{t>t_{tail}} W_{out}^2(t)$$

the tail being defined as the signal portion after the time t_{tail}.

In particular, to obtain the calibration board parameters, τ_{cali} and f_{step}, a step function will be chosen for $Y_{inj}(t)$, and to extract τ_0 a cosine function for $Y_{inj}(t)$ is more suitable.

Extraction of the calibration boards parameters: τ_{cali} and f_{step}

To obtain the calibration pulse parameters τ_{cali} and f_{step} a step function, $Y_{inj}(t) = \theta(t)$, is used with unit amplitude. The Laplace transform of the step function is $Y_{inj}(s) = 1/s$. On the other hand, the expression for $I_{inj}^{cali}(s)$, seen in previous section, can be written, for unit amplitude, as:

$$I_{inj}^{cali}(s) = \frac{\tau'_{cali}s + f'_{step}}{s(1+\tau'_{cali}s)}$$

Hence, the ratio between both injection signals is:

$$\frac{Y_{inj}(s)}{I_{inj}^{cali}(s)} == \frac{1+s\tau'_{cali}}{s\tau'_{cali} + f'_{step}}$$

and W_{out} can be obtained as:

$$W_{out}(s) = \frac{1+s\tau'_{cali}}{s\tau'_{cali} + f'_{step}} g^{cali}(s)$$

It can be shown that, for the correct values $\tau'_{cali} = \tau_{cali}$ and $f'_{step} = f_{step}$ of the calibration board parameters, $W_{out}(t)$ has the property of going to zero in the tail very

rapidly. This is due to the fact that both H^{det} and $H^{readout}$ functions contain only short time constants and do not give rise to a long tail in the waveform.

This null-tail property of the step-response can be used to determine both calibration board parameters by minimizing the following quantity:

$$Q^2(\tau'_{cali}; f'_{step}) = \sum_{t>t_{tail}} W^2_{out}(t; \tau'_{cali}; f'_{step})$$

The minimization procedure may in principle depend on the tail starting point value t_{tail}. A robust choice of t_{tail} is given by $t_{tail} = t_{min} + 100ns$, where t_{min} is the minimum of the negative lobe of the shaped signal [1]. Using this criterion the systematic error introduced by t_{tail} in the RTM procedure is small.

Extraction of the detector parameters: τ_0 and τ_r

To extract τ_0, or equivalently $\omega_0 = 1/\tau_0$, the response to a monochromatic cosine pulse $Y_{inj}(t) = \theta(t)cos(\omega t)$ is studied, which, in the Laplace frequency domain, has the form:

$$Y_{inj}(s) = \frac{s}{s^2 + \omega^2}$$

The ratio between both "cosine-type" and calibration injection signals is:

$$\frac{Y_{inj}(s)}{I^{cali}_{inj}(s)} == \frac{s}{s^2 + \omega^2} \frac{s(1 + s\tau_{cali})}{s\tau_{cali} + f_{step}}$$

and W_{out} can be obtained as:

$$W_{out}(s) = \frac{s}{s^2 + \omega^2} \frac{s(1 + s\tau_{cali})}{s\tau_{cali} + f_{step}} g^{cali}(s)$$

It turns out that the smallest amplitude for this function is obtained when $\omega = \omega_0$, hence this parameter is obtain by minimizing the following quantity:

$$Q^2(\omega) = \sum_{t>t_{tail}} W^2_{out}(t; \omega) \times \frac{(1 + (\omega\tau_{sh})^2)^3}{(\omega\tau_{sh})^2}$$

[1] One can look at figure 4.1 to see the negative lobe of the shape signal, although the pulse shape corresponds to a ionization signal instead of a calibration step function

where the last term introduces a shaper correction in this case, due to the fact that the shaper acts as a band-pass filter suppressing the high frequency components of the injected signals.

Finally the parameter τ_r can be extracted by injecting $Y_{inj} = I_{inj}^{cali}$, however at the physics injection point. This introduces a correction factor in the output signal, which depends on τ_r' as follows:

$$\frac{1}{1+s\tau_r'+s^2\tau_0'}$$

Hence,

$$W_{out}(s) = \frac{1}{1+s\tau_r'+s^2\tau_0'} g^{cali}(s)$$

If $\tau_0' \neq \tau_0$ or $\tau_r' \neq \tau_r$ the function $W_{out}(t)$ will have an oscillating behavior on the tail. We can assume that τ_0 has been obtained before by the RTM method, as described in previous subsection, or by direct measurements. Hence, the quantity to minimize in order to obtain τ_r is defined as:

$$Q^2(\tau_r') = \sum_{t>t_tail} (W_{out}(t;\tau_r') - g^{cali}(t))^2$$

Chapter 5

Signal reconstruction in the end-caps

The first section of this chapter synthesizes the present knowledge of the input parameters needed to compute the optimal filtering coefficients for the end-caps. As a first cross-check, and wherever it is relevant, these inputs are compared to the EM barrel ones. The outputs of the method, *i.e.* the predicted physics pulse shapes, the optimal filtering coefficients, the calibration bias and the noise reduction, are discussed in section 5.2.

5.1 Inputs for the end-caps

5.1.1 Cell response to a calibration signal

Typical shapes of cell responses to a same calibration input are shown in Figure 5.1 (left) for the three EMEC layers. The differences between shapes are explained by the electrical characteristics of each layer. Notice that, in the finely segmented part of the front sampling, $1.5 < \eta < 2.4$, the crosstalk between neighbor cells is important, between 3 and 5% [21], and has been taken into account by adding the two neighboring cell shapes to the pulsed one. As a global sanity check, the dispersion along ϕ of the maximum amplitude of all calibration shapes is shown to be the same for all layers and exhibits no dependency as a function of η (Figure 5.1, right).

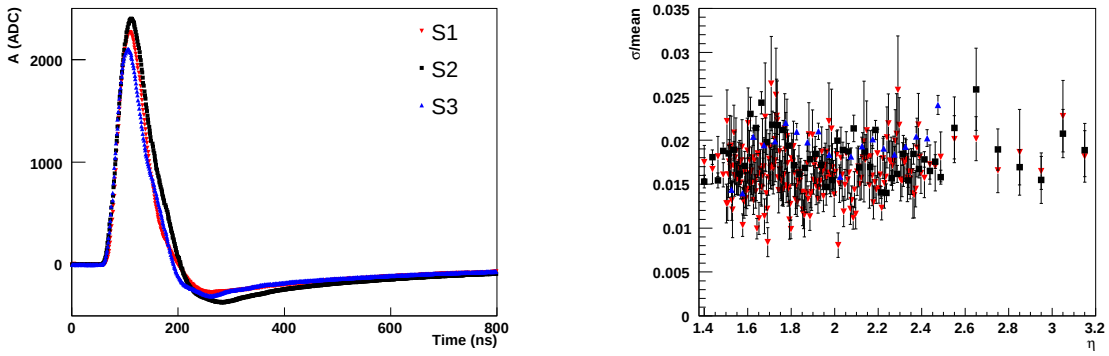

Figure 5.1: *Left: Typical calibration pulse shapes at* $\eta = 1.8$ *for an input of 500 DAC units in high gain. Right: Dispersion over* ϕ *of the maximum amplitude of all calibration shapes in high gain, as a function of* η*. Front, middle and back cells are represented with red down triangles, black squares and blue up triangles, respectively.*

5.1.2 Calibration board parameters

To obtain an efficient calibration, the input signal should be as similar as possible to the ionization triangular pulse. Two main parameters, τ_{cali} and f_{step}, are needed to describe this calibration input pulse:

$$I_{inj}^{cali}(t) = I_0^{cali} \cdot \theta(t) \cdot \left[(1 - f_{step})e^{-\frac{t}{\tau_{cali}}} + f_{step}\right] \tag{5.1}$$

where $\theta(t)$ is the unit step function. The exponential decay time τ_{cali} is chosen to mimic the decay slope of the ionization signal, while f_{step} is related to the resistive component of the inductance in the calibration board [11].

These two parameters need to be known for every calibration board channel. They can be extracted from measurements in the production laboratories [22] or can be inferred from the cell response to a calibration pulse using the Response Transformation Method (RTM) [11]. Figure 5.2 shows a comparison between the two methods for both parameters of one calibration board. Relative systematic shifts of -7% and $+15\%$ using RTM compared to the measured values are observed for extracted τ_{cali} and f_{step}, respectively, which is as expected in very good agreement with what was already reported for the barrel. This is probably because RTM gives effective parameters, absorbing for instance attenuation effects [23, 24]. As not all calibration board measurements were available, the RTM extracted parameters are chosen to be consistent. Notice that choosing the RTM extracted parameters impacts only the absolute energy scale, which can not be tested very precisely with cosmic data.

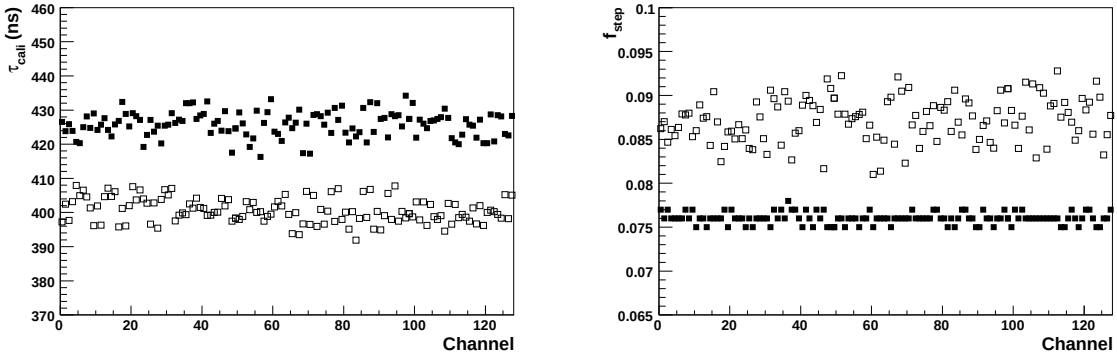

Figure 5.2: *Comparison of τ_{cali} (left) and f_{step} (right) extracted by RTM (open symbols) and measured directly (closed symbols) for the 128 channels of one calibration board.*

5.1.3 Ion drift time in liquid argon gap

The ion drift time in liquid argon gap, t_{drift}, can be expressed in terms of applied high voltage U and gap thickness g [26]:

$$t_{drift} = \frac{g}{V_{drift}} \sim \frac{g^{b+1}}{U^b} \tag{5.2}$$

where $b \sim 0.4$ is a parameter first determined with specific measurements [26] and then crosschecked with beam tests [27, 28, 29]. As indicated in section 3.2, the complicated EMEC geometry implies a variation of the gap thickness along η, which induces a varying drift time despite the change in the high voltage. This is a major difference with the barrel part, for which the drift time is almost constant around 470 ns for $U = 2000$ V.

The drift time can be computed using Equation (5.2) or extracted from a fit to the physic pulse shapes recorded with test-beam data [1] [28], with a precision estimated around 10%. Figure 5.3 shows the measured t_{drift}, averaged over ϕ, as a function of η for all EMEC layers [2]. They are in good agreement with the predictions extracted from Equation (5.2). Notice that any change on HV setting conditions implies a change of the drift time in the corresponding region.

[1] At the beam tests, as events are asynchronous with respect to the clock, the 5 sample physics pulse in a cell can be averaged within a 1 ns bin by using the phase of each event.

[2] No measurement was available in the region $1.4 < |\eta| < 1.6$, in which the prediction is therefore taken.

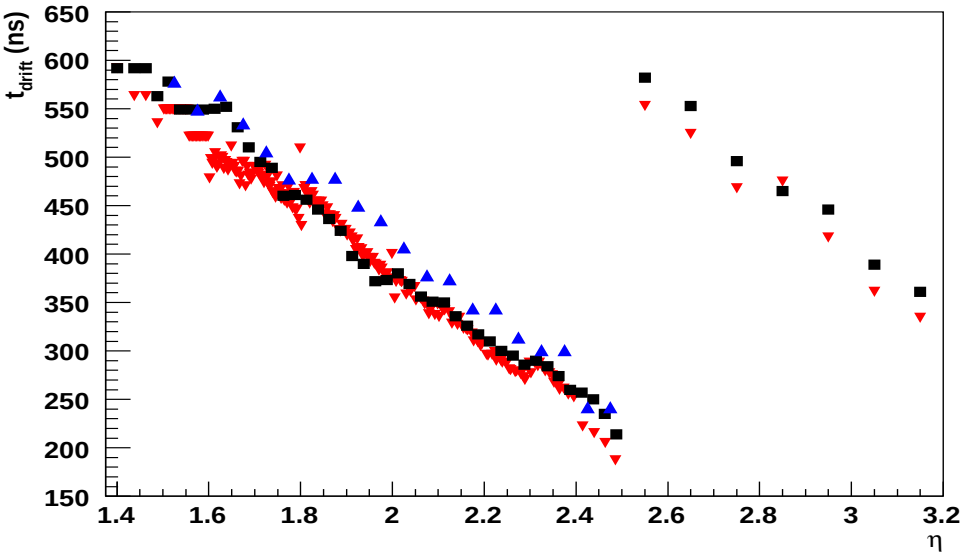

Figure 5.3: *Drift time as a function of* η *for front (red down triangles), middle (black squares) and back (blue up triangles) end-cap layers. All points have been averaged over* ϕ.

5.1.4 Electronic chain characteristics

A thorough program of measurements was carried out at cold on all cells of the EMEC calorimeter before installation of the front end electronics to measure their electrical properties as precisely as possible. By means of a Network Analyser [22], a frequency scan was performed to extract precisely the resonance frequency of the cell circuit $\omega_0 = 2\pi\nu_0 = 1/\tau_0 = 1/\sqrt{LC}$ and the product $\tau_r = rC$. In both cases, the most precise measurements were obtained in the second layer (first layer in the inner wheel), where capacitances are higher. Results are more difficult or impossible to extract in the first and third layers, and the approximation $\tau_0 = \tau_r = 0$ is therefore used in the following for these samplings.

Resonance frequency

Typical examples of end-cap S2 cell responses to a frequency scan with a Network Analyser are shown in Figure 5.4 (top). The resonance frequency is clearly visible on the left-hand plot, and is obtained by fitting a parabola around the minimum. The determination of the resonance frequency can be complicated by the presence of reflections near the peak, as illustrated in the second column of Figure 5.4 (top). This situation is even more pronounced when the resonance frequency is higher, *i.e.* the capacitance and the inductance are low, as for example at high η in the EMEC outer wheel (fourth column of Figure 5.4 top). In the last two cases, the resonance frequency is inferred by fitting the edges of the two minima with straight lines and computing the intercept point of both

lines. To partly overcome this problem, ω_0 is not measured for every cells but averaged over ϕ at every η. Results are shown in Figure 5.5 (closed symbols). Their η-dependency, qualitatively reproduced by individual measurements of L and C [30], reflects the decrease of L and C as a function of η. This has to be compared to the barrel case, with a ω_0 varying only between 0.13 and 0.19 GHz [22].

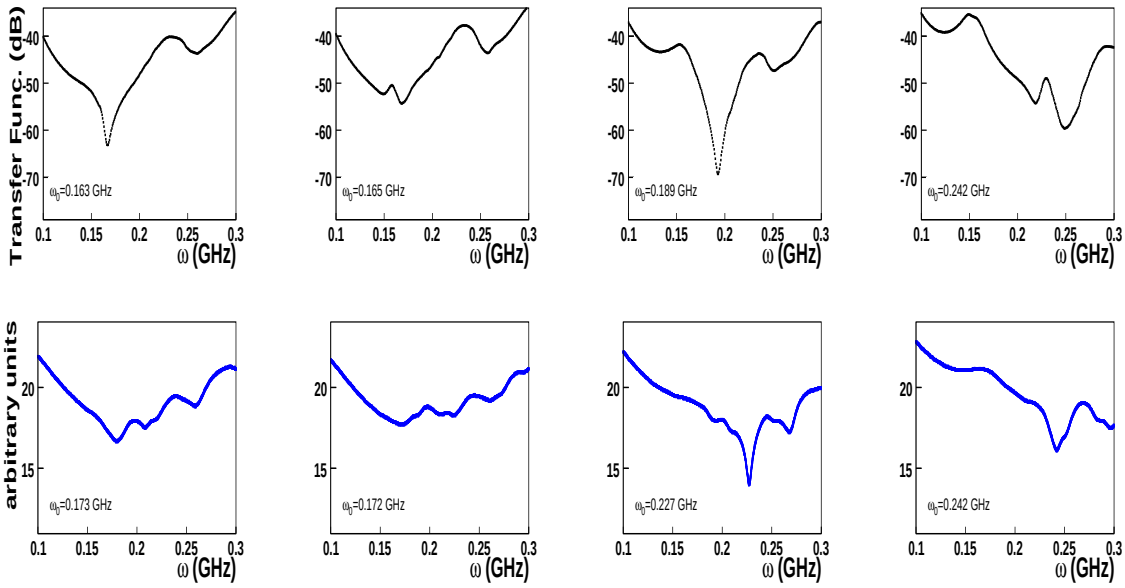

Figure 5.4: *Typical S2 cell responses in the 100-300 MHz frequency range at* $\eta = 1.6$ *(first row),* $\eta = 1.7$ *(second row),* $\eta = 1.8$ *(third row) and* $\eta = 2.2$ *(fourth row), as measured with a network analyser (top) and with the RTM method (bottom).*

Because of the uncertainties in the resonance frequency measurement described above, it is desirable to extract ω_0 with an alternative method, *i.e.* RTM in this case. The corresponding output functions [3] are illustrated for the same cells as for the measurements in Figure 5.4 (bottom). In all cases, comparable results with measurements are obtained, apart in the third column where the resonance frequency is 20% higher. Figure 5.5 shows RTM and measurement results as a function of η in S2. The agreement is good in the regions with high capacitances ($\eta < 1.7$ and $\eta > 2.5$), close to the barrel situation [4]. The situation worsens in the regions with lower capacitances, *i.e.* $1.7 < \eta < 2.5$, where the disagreement between RTM and measurements can reach up to 10-15%. To study the systematic effect on energy measurement linked to this disagreement, the two different ω_0 sets are considered in the following. Results are presented in details in section 7.2.3.

[3] The resonance frequency corresponds to the minimum of the function.

[4] The agreement between measurements and RTM extracted values at combined test-beam was $\sim 1\%$ for S2, well compatible with the precision required [14].

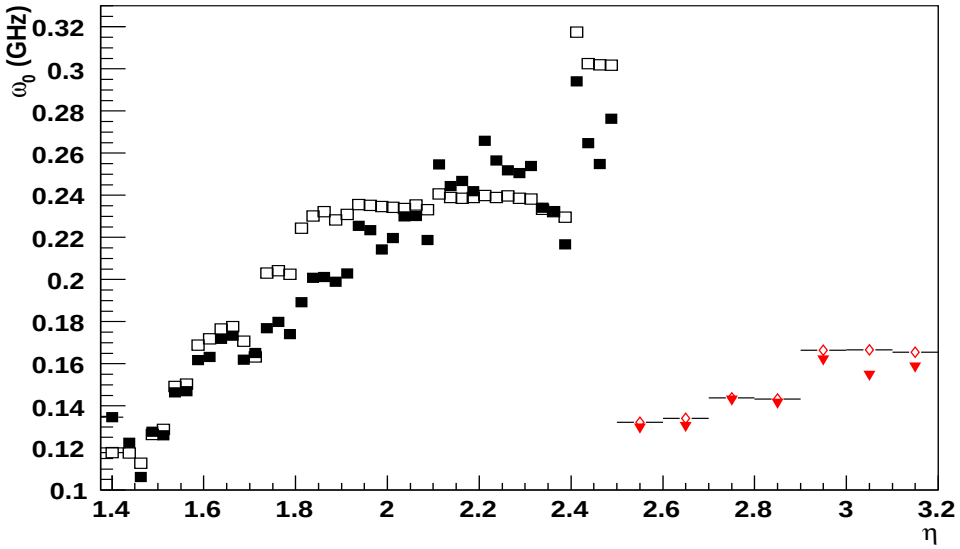

Figure 5.5: *Cell resonance frequency* ω_0 *obtained with network analyser measurements (closed symbols) and extracted with RTM (open dots), as a function of* η *for S2 cells (S1 in inner wheel). All points have been averaged over* ϕ*.*

rC measurement

The product $\tau_r = rC$ can be determined by measuring r and C separately. The r values can be extracted from the frequency scan measurements by looking at the pulse amplitude at the resonance frequency [22], whereas C can be taken from direct measurements performed after EMEC module stacking [30]. Figure 5.6 shows the τ_r values obtained by this method as a function of η. As for the resonance frequency, it is desirable to compare these measurements with the values extracted by RTM : a large disagreement is obtained, with measurements lower than RTM values by a factor ~ 5 (Figure 5.6). This is because RTM gives effective parameters, *i.e.* absorb some additional effects not considered in the LAr readout model [25]. Similar observations are made in the barrel, with a factor between RTM and measurements of $\sim 2-3$ [32]. However, the impact on the amplitude determination is very small [11], and the measurements can not be used to predict the physics shapes, as it generates residual oscillations in the tails [25]. This is illustrated in Figure 5.7 in the end-cap case, and is similar for the barrel. As a consequence, RTM extracted values will be used in the following.

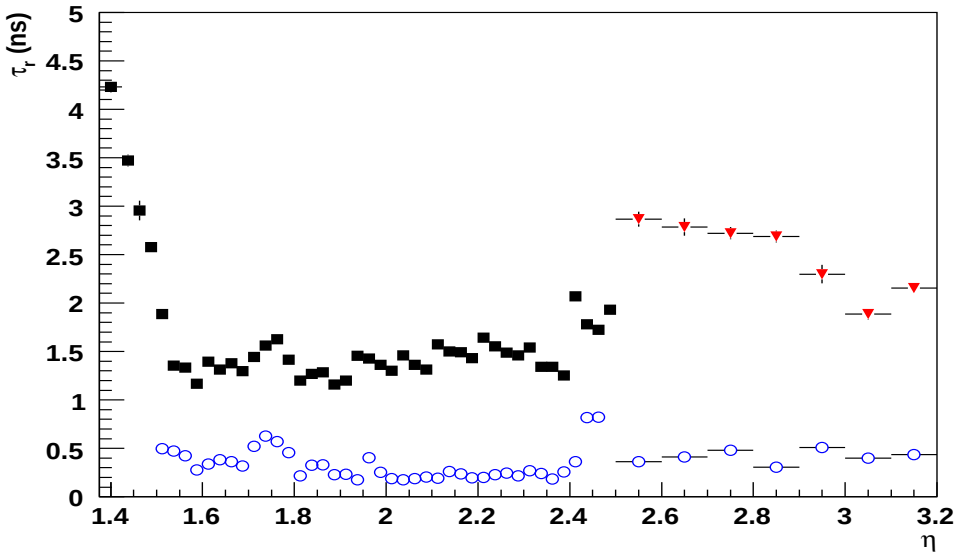

Figure 5.6: *Comparison of cell τ_r computed from the product of the measured r and C (open symbols) and extracted with RTM (closed symbols), as a function of η for S2 cells (S1 in inner wheel). All points have been averaged over ϕ.*

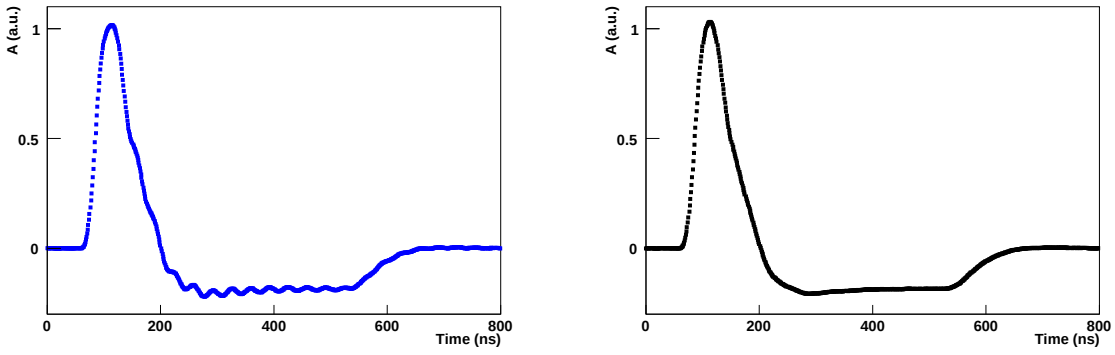

Figure 5.7: *Typical predicted physics pulse shape computed with measured τ_r (left) and RTM τ_r (right) at $\eta = 1.8$.*

5.1.5 Summary of the inputs

Except t_{drift}, all input parameters for signal reconstruction in the end-caps have been either directly measured or inferred from calibration system through RTM method. The choice made between both has been discussed in the previous sections. The situation is very similar to the barrel case for the calibration board parameters f_{step} and τ_{cali}, as well as for τ_r. It is different for ω_0 in the regions with a high resonance frequency ($1.7 < \eta < 2.5$), which renders the measurement difficult. To estimate the impact of a mismeasurement of this parameter, two sets of input parameters are considered, which can further serve to estimate the related systematic uncertainties on signal reconstruction (section 7.2.3). Table 5.1 summarizes the origin of the input parameters used to predict the physics pulse shapes in the end-caps. The ω_0 set coming from direct measurements will serve as reference in the following, and therefore used unless otherwise stated.

	Outer Wheel			Inner Wheel	
Parameter	S1	S2	S3	S1	S2
f_{step}	RTM	RTM	RTM	RTM	RTM
τ_{cali}	RTM	RTM	RTM	RTM	RTM
t_{drift}	meas.	meas.	meas.	meas.	meas.
τ_r	0	RTM	0	RTM	0
ω_0 - Reference	0	meas.	0	meas.	0
ω_0 - Set 2	0	RTM	0	RTM	0

Table 5.1: *Origin of input parameters used for signal reconstruction in the end-caps. RTM refers to the Response Transformation Method [11], which infers the parameters from the cell response to a calibration pulse. Meas. refers to extensive measurements performed before the installation of the front end electronics. The two ω_0 sets will be used to compute the two sets of optimal filtering coefficients later tested in the cosmic muon run analysis (section 7).*

5.2 Outputs of the method

5.2.1 Computation of the pulse shapes and optimal filtering coefficients for physics

All input parameters discussed in section 5.1 enter directly in Equation (4.6) to predict the physics pulse shape of each EMEC cell. Typical shapes can be seen in Figure 5.8 (left) for the three EMEC layers. As a first check on the quality of this prediction, the dispersion along ϕ of the maximum amplitude is shown as a function of η for the three layers in Figure 5.8 (right). It is roughly constant below 0.1% for S1 and S3 in the precision region ($1.5 < |\eta| < 2.5$). It decreases with η in S2, following the τ_0 variation [5]. Notice that the same results are obtained with the two ω_0 input sets of Table 5.1. More quantitative checks of the quality of these predicted shapes are proposed in section 7.2.2 using cosmic data.

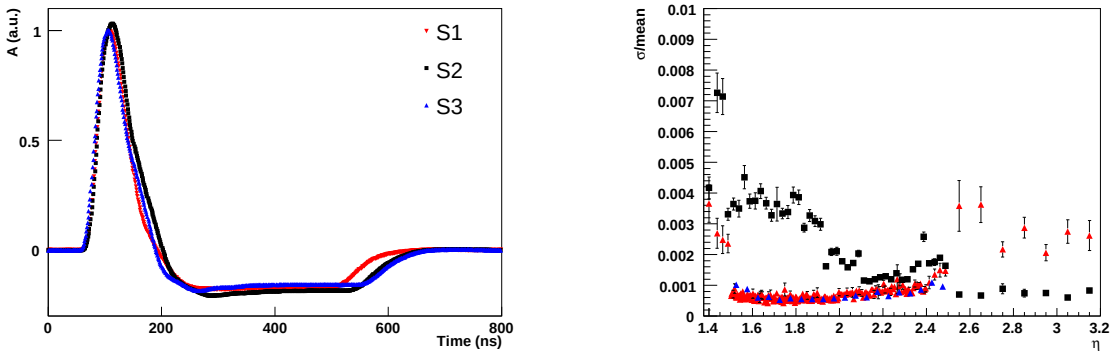

Figure 5.8: *Left: Typical predicted physics shape at* $\eta = 1.8$ *in high gain. Right: Dispersion over* ϕ *of the maximum amplitude of all physics shapes in high gain, as a function of* η. *Front, middle and back cells are represented with red down triangles, black squares and blue up triangles.*

From these physics pulse shapes and their derivatives, optimal filtering coefficients (OFC) a_i and b_i are computed per cell for each gain and for 50 phases by 1 ns step. This has been done with 5 or 25 samples and using one of the two input parameter sets of Table 5.1. Unless otherwise stated, the case with 5 samples and reference input set is used in the following.

[5] It was checked that using $\tau_0 = \tau_r = 0$ in S2, results become similar to S1 and S3.

5.2.2 Estimation of the calibration bias

The difference between physics and calibration shapes induces a different response amplitude to a normalized input signal. The resulting bias must be taken into account in order to correctly convert ADC counts into energy. This is achieved by using the ratio between the maximum amplitudes of physics and calibration pulses, called $\frac{M_{phys}}{M_{cali}}$. It is shown in Figure 5.9 as a function of η for the 3 EMEC layers in high gain [6]. The decreasing behavior with η reflects at first order the cell inductance variation [30] (mainly visible for S2), and at second order the drift time variation (visible for S1 and S3 where the inductance is assumed to be zero, $\tau_0 = \tau_r = 0$).

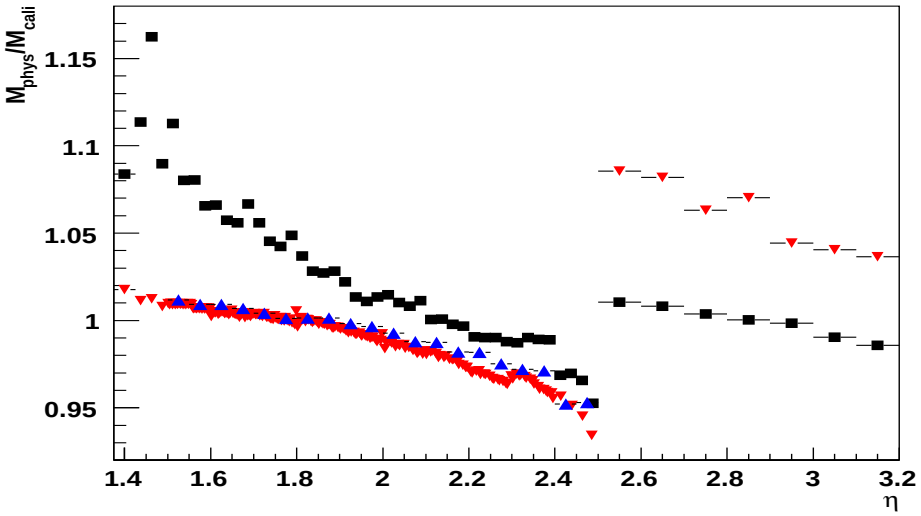

Figure 5.9: *Bias in the signal reconstruction method* $\frac{M_{phys}}{M_{cali}}$ *in front (red down triangles), middle (black squares) and back (blue up triangles) EMEC cells. All points have been averaged over* ϕ*. High gain and the reference input set of Table 5.1 are used.*

A comparison with $\frac{M_{phys}}{M_{cali}}$ values obtained with 2001-2002 test beam analysis [13] is proposed in Figure 5.10 (left). The differences are quite important, at the level of $5-8\%$ in the region $1.5 < \eta < 2.4$, reflecting the different conditions of both analyses and data takings : cable lengths, optimal filtering coefficient computations, calibration and front-end electronics, etc. As a systematic check, it is interesting to make the same comparison between the two ω_0 input sets of Table 5.1. The agreement is at the percent level, as shown in Figure 5.10 (right). Finally, notice that the prediction of this bias on the signal reconstruction method can hardly be checked with commissioning data, since the absolute muon energy scale is only known at $\sim 5\%$ [15]. The uncertainties on $\frac{M_{phys}}{M_{cali}}$ ratio

[6] It was checked that the gain has no impact on the ratio.

will later be absorbed in the inter-calibration coefficients extracted with electrons from Z decay [31].

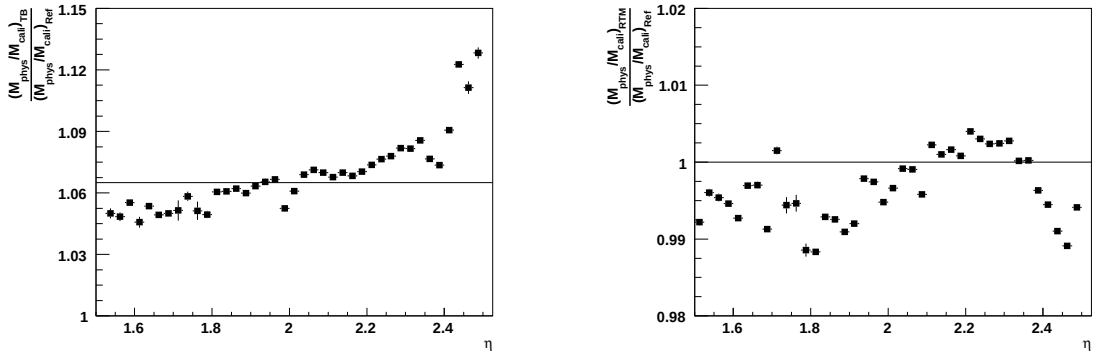

Figure 5.10: *Ratios of $\frac{M_{phys}}{M_{cali}}$ in S2 between the present analysis with the reference set and 2001-2002 test beam analysis [28] (left) and between the two ω_0 input sets of Table 5.1 (right).*

5.2.3 Noise reduction with optimal filtering technique

The computation of the optimal filtering coefficients (OFC) is performed to minimize the noise contribution to the signal reconstruction. To check this noise reduction, the OFC are applied to pedestal runs for different number of samples. The noise level obtained using 5 samples in high gain, averaged over ϕ, is shown in Figure 5.11 for the three EMEC layers as a function of η. In the precision region $1.5 < \eta < 2.5$, weak variations are observed along η and average noise values of 14, 32 and 27 MeV are measured for the three samplings, respectively. This agrees nicely with the module test-beam results [27].

The noise reduction obtained with optimal filtering technique increases with the number of samples used, as more signal information is available and the noise correlation between samples is better accounted for. This is illustrated in Figure 5.12 at $\eta = 1.8$ for the three layers. Reduction factors of 1.5 (1.4) and 2.4 (2.2) are obtained in the second (first) layer using 25 samples compared to 5 and 1, respectively. These results are slightly lower than those obtained in the barrel, $\sim$1.8 (1.8) and $\sim$2.9 (2.6) [15] because of lower capacitances in the end-cap. Figure 5.13 shows the noise reduction in S2 as a function of η using 5 (left) and 25 (right) samples with respect to one single sample. Smooth behaviors are observed in the regions $1.5 < \eta < 2.5$ and $2.5 < \eta < 3.2$. The more pronounced variation for 25 samples is at first order a consequence of the drift time variation (Figure 5.3) : a lower drift time gives a shorter waveform. As a consequence, the number

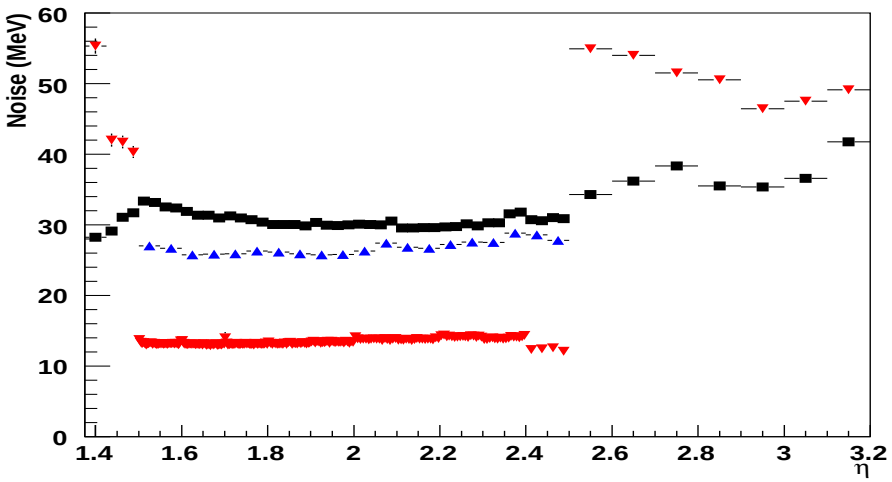

Figure 5.11: *Total noise computed with 5 samples OFC in high gain, averaged over* ϕ *and as a function of* η*, for front (red down triangles), middle (black squares) and back (blue up triangles) EMEC cells.*

of meaningful samples decreases with η, degrading the reduction factor brought by the optimal filtering technique.

It is interesting to notice that these results on noise can serve as a benchmark to check the computation of the physics OFC, and can also point to a wrong latency setting of the read-out [33]. They therefore give confidence on the quality of the data taking set-up and of the autocorrelation matrix and OFC computation. This allows to go further, and perform an analysis of the small signals deposited by cosmic muons over the complete calorimeter coverage, $0 < \eta < 3.2$. This is the subject of the next section.

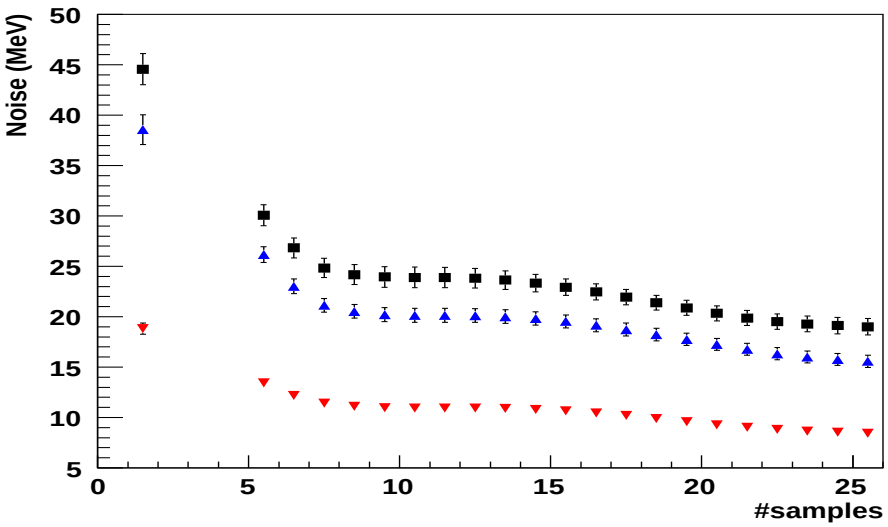

Figure 5.12: *Noise as a function of the number of samples used by optimal filtering for the three EMEC layers in high gain at* $\eta = 1.8$*. Front, middle and back cells are represented with red down triangles, black squares and blue up triangles.*

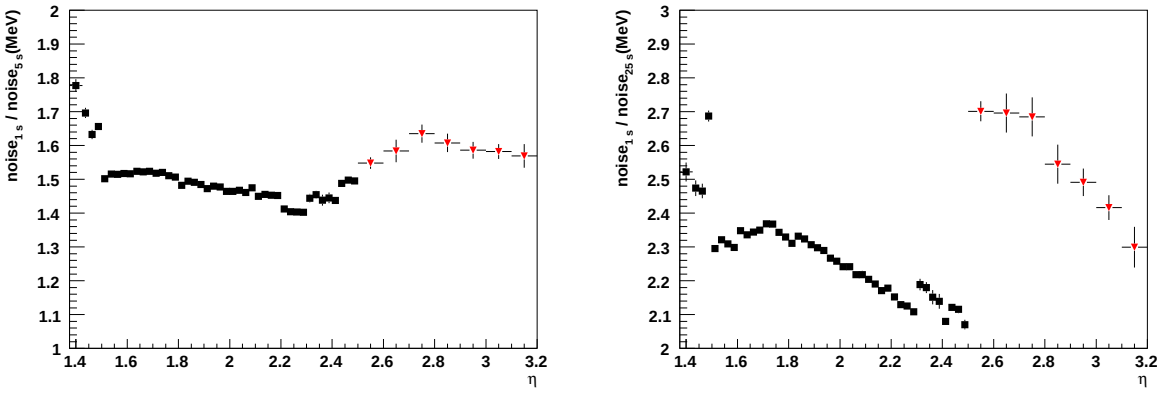

Figure 5.13: *Noise reduction as a function of* η *in S2 (resp. S1) of the outer (resp. inner) wheel using 5 samples (left) and 25 samples (right) OFC, compared to one single sample.*

Chapter 6

Cosmic runs

6.1 Origin of cosmic muons

Cosmic rays are energetic particles originating from space that impinge on Earth's atmosphere. Almost 90% of all the incoming cosmic ray particles are protons, about 9% are helium nuclei and about 1% are electrons. The sources are the Sun, galactic objects like neutron stars, supernovas, etc, and extragalactic objects. Cosmic rays can have energies of over $10^8 TeV$, far higher than the $7TeV$ of the LHC.

When cosmic ray particles enter the Earth's atmosphere they collide with molecules, mainly oxygen and nitrogen, to produce a cascade of lighter particles, a so-called air shower. The general idea is shown in figure 6.1 which shows a cosmic ray shower produced by a high energy proton of cosmic ray origin striking an atmospheric molecule. The figure is a simplified picture of an air shower for the sake of clarity.

All of the produced particles stay within about one degree of the primary particle's path. Typical particles produced in such collisions are charged mesons, pions and kaons, which may decay into muons. Since muons interact weakly with the atmosphere, they may reach the Earth ground, hence they can be used for detector calibration studies as in the present work. The energy spectrum of cosmics muons is shown in figure 6.2.

The rest of the particles of the air shower are, sooner or later, absorbed by the atmosphere.

6.2 Energy loss due to ionization

Let us consider a heavy particle, with charge ze, mass M and velocity v traversing a block of matter. Let us assume that at a distance b of the incident particle direction an atomic

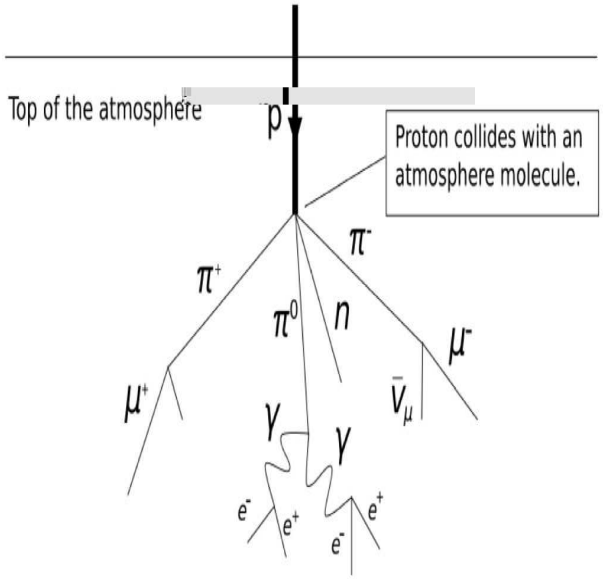

Figure 6.1: Interaction of a cosmic proton with an air molecule.

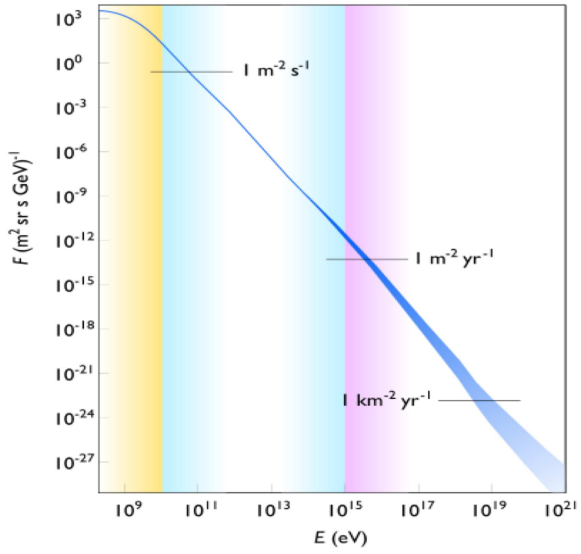

Figure 6.2: Muon flux as a function of the muon energy

electron is found. One can use a semi-classical approximation assuming the electron to be free and at rest during the time the interaction takes place. One usually further assumes that the direction of the incident particle is not changed as it is much heavier than the atomic electron.

General case: the Bethe-Bloch formula

Within these approximations, Bohr obtained expressions for energy loss of heavy particles (α particles of heavy nuclei), which were found to properly describe experimental data. For lighter particles like protons a disagreement with experiment was found, because quantum effects were not taken into account. The correct quantum-mechanical calculation was first performed by Bethe and Bloch, obtaining this formula:

$$-(\frac{dE}{dx})_{ioniz} = 2\pi N_a r_e^2 m_e c^2 \rho \frac{Z}{A}\frac{z^2}{\beta^2}\left[\ln\left(\frac{2m_e\gamma^2 v^2 W_{max}}{I^2}\right) - 2\beta^2\right]$$

where:

E : incident particle energy
x : path length
N_a : Avogadro's number ($6.022 \times 10^{23} mol^{-1}$)
r_e : classical electron radius (2.817×10^{-13}cm)
m_e : electron mass
ρ : density of absorbing material
A : atomic weight of absorbing material
Z : atomic number of absorbing material
z : charge of incident particle in units of e
β : v/c of the incident particle
γ : $1/\sqrt{(1-\beta)}$
W_{max} : maximum energy transfer in a single collision
I : mean excitation potential

In practice, two more corrections are needed, the so called density effect and the shell effect [7]:

$$-(\frac{dE}{dx})_{ioniz} = 2\pi N_a r_e^2 m_e c^2 \rho \frac{Z}{A}\frac{z^2}{\beta^2}\left[\ln\left(\frac{2m_e\gamma^2 v^2 W_{max}}{I^2}\right) - 2\beta^2 - \delta - 2\frac{\zeta}{Z}\right] \quad (6.1)$$

where:

- δ: density effect correction, which arises from the fact that the electric field of the particle also tends to polarize the atoms along its path.

- ζ: shell effect correction, which accounts for effects when the velocity of the incident particle is comparable or smaller than the orbital velocity of the bound electrons.

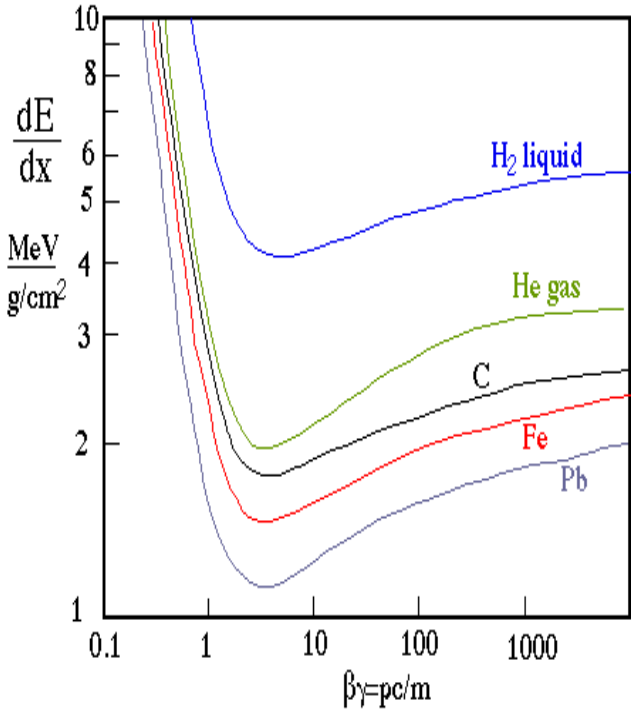

Figure 6.3: Ionization energy loss per unit of length in liquid hydrogen, gaseous helium, carbon, iron and lead.

The maximum energy transfer occurs in head on collisions between the incident particle and the atomic electron has the expression:

$$W_{max} = \frac{2m_e c^2(\beta\gamma)^2}{1+2s\sqrt{1+(\beta\gamma)^2}+s^2}$$

with $s = m_e/M$.

A semi-empirical formula can be used for the excitation potential, namely:

$\frac{I}{Z} = 12 + \frac{7}{Z} eV \qquad Z < 13$

$\frac{I}{Z} = 9.76 + 58.8\, Z^{-1.19} eV \qquad Z \geq 13$

which gives a reasonable approximation for most cases.

The energy loss per unit length depends on the energy of the incident particle. It exhibits a sharp fall off, proportional to $1/\beta^2$ for low β values, it reaches a minimum known as the ionization minimum (around $\beta\gamma = 3$), and finally shows a logarithmic increase (relativistic rise) leading to a plateau (*the Fermi plateau*), see figure 6.3. For energies bigger than the ionization minimum, each particle shows a characteristic curve. It can be used to identify particles in this energy range.

Cosmic muons lose energy in the EM calorimeter primarily through ionization. The mean energy loss (E) is given by equation 6.1, hence E is proportional to the path length (x) crossed by the muon. Event by event this energy is subjected to stochastic fluctuations described by a Landau distribution. This function is not symmetric exhibiting a characteristic tail at high energy losses, hence the mean value of the distribution differs from the Most Probable Value (MPV). In practice, the MPV is more relevant than the mean value, for example for calibration studies, since the tail is often difficult to define with enough precision. It can be shown that the MPV is related to the path length through an relation of the type $MPV \sim x(a + \ln x)$, although the logarithm is usually much smaller than the term a, hence may be neglected in those cases. In addition, the ratio ω/MPV, where ω is the full width at half maximum of the Landau distribution, decreases when x increases.

6.3 Energy loss by radiation: Bremsstrahlung

If a charged particle is decelerated in the Coulomb field of a nucleus a fraction of its kinetic energy will be emitted in form of real photons (bremsstrahlung). The electron and positron are the only particles for which energy loss by bremsstrahlung is significantly important, see figure 6.4 for a diagrammatic representation.

In fact the semi-classical calculation for the bremsstrahlung cross-section for any given particle of mass M reads [8]:

$$\left(\frac{d\sigma}{dk}\right)_{rad} \simeq \frac{5e^2}{\hbar c} z^4 Z^2 \left(\frac{m_e c}{Mv}\right)^2 \frac{r_e^2}{k} \ln\left(\frac{Mv^2\gamma^2}{k}\right)$$

with k the energy of the produced photon.

It can be seen that the dependence of the previous cross section with the particle mass M is (neglecting the logarithm term):

$$\left(\frac{d\sigma}{dk}\right)_{rad} \propto M^{-2}$$

Thus, the bremsstrahlung cross-section for a muon, M_μ =105.7 MeV, is approxi-

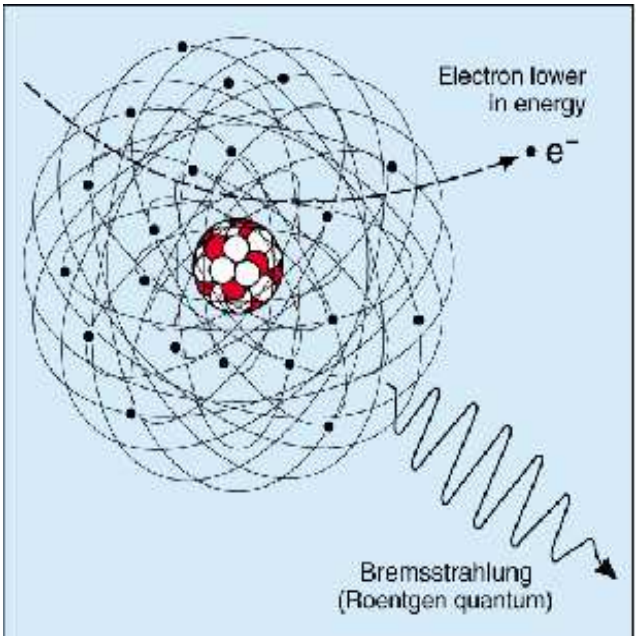

Figure 6.4: Feynman diagram for bremsstrahlung.

mately 44000 times smaller than that for an electron, m_e =0.51 MeV. Despite of this fact bremsstrahlung of muons has been observed in the ATLAS EM calorimeter; actually these are the type of events mostly used in the present analysis.

We can also note in the formula that the cross-section is proportional to Z^2, i.e. to the atomic number squared of the traversed material. This explains the use of high Z materials (Fe, Cu, Pb, U) as absorbers in sampling calorimeters, in order to get a bigger energy loss by radiation. Finally, the cross-section becomes very large as the radiated photon becomes very soft (k very small).

Up to now we have only dealt with the interaction of the incident particle with the nuclear Coulomb field. One has to take into account the screening effect due to the atomic electrons, which changes the cross section formula slightly. Details can be found in [9].

6.4 Calorimeters setup for cosmic runs

In 2006, ATLAS entered the ”in situ” commissioning phase. The primary goal of this phase is to verify the detector operation and performance using cosmic muons. All ATLAS sub-detectors are presently in the last stage of installation in the cavern at Point 1 of the LHC accelerator. After the installation of each sub-detector, extensive testing (commissioning) has been performed.

In the first phase of the commissioning, the proper functionality of the detectors has been verified in a stand-alone mode. In the next phase, the different sub-detectors were integrated into the common data acquisition, monitoring, detector control and safety ATLAS system frameworks. The process of integrating more and more sub-systems has been ongoing since summer 2006 when the first common partition between the Liquid Argon (LAr) barrel electromagnetic (EMB) calorimeter and the hadronic Tile barrel calorimeter was created. At the beginning of 2007, the End-Cap A electromagnetic calorimeter (EMEC A) and the extended barrel part at $0.8 < \eta < 1.7$ for the Tile calorimeter (see chapter 2) were incorporated to this partition.

The analysis of cosmic muon events is the only way to test the EM calorimeter in situ with physics signals before LHC collisions. During the summer 2007, the situation for Barrel and End-Cap-A liquid Argon calorimeters was stable and the cosmic data were taken nearly every weekend. An example of a cosmic muon event crossing the barrel ATLAS calorimeters is given in figure 6.5. The energy deposited in the Hadronic Tile Calorimeter (in blue) and the Electromagnetic Calorimeter (in white) can be well distinguished. There is a clear matching of the different cells with energy deposits, being a projective muon crossing the center of the ATLAS detector.

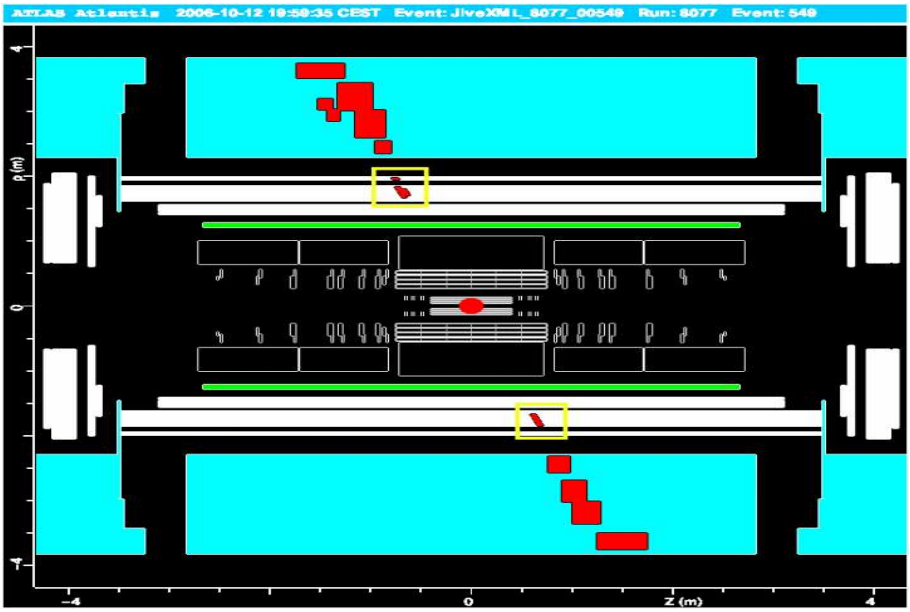

Figure 6.5: Display of a cosmic muon crossing the ATLAS Barrel Calorimeters, obtain using the Atlantis display program. The Hadronic Tile Calorimeter is represented in blue, while the Electromagnetic Calorimeter appears in white color.

A dedicated trigger using only Tile calorimeter signals was configured to detect cosmic muons in the electromagnetic calorimeter. In the following chapter, the data taking

conditions for cosmic runs used in this analysis will be explained in more detailed. However, it is important to understand the complicated situation for the end-cap part respect to the barrel one. Figure 6.6 shows the Tile towers [1] that were included in the trigger for the data taking. The Hadronic Tile Calorimeter is represented in green in the figure, while the Electromagnetic Calorimeter (Barrel + two End-Caps A and C) is in brown. The best trigger situation for detecting muons in the end-cap A side would be using EBA top and bottom as a trigger. However these muons are not projective to the ATLAS center, which means they do not cross the EMEC cells along the cell depth, hence the average energy deposited by ionization is too tiny to be detected. Only Landau fluctuations could make a small fraction of events to leave a measurable signal, useful for the analysis. On the other hand, bremsstrahlung photons, of sufficient energy, emitted by cosmic muons can be detected since the photon initiates an electromagnetic cascade in the EMEC, "lighting" several cells in the same event. As seen in previous section, the probability for the bremsstrahlung process in muons is tiny, due to its large mass. Hence the number of muon events selected for calibration of the EMEC is small. One of these events can be seen in the Atlantis display of figure 6.7. Both top and bottom EBA Tile towers are triggered and a small spot in the EMEC is seen, which corresponds to the small electromagnetic cascade created by the bremsstrahlung photon.

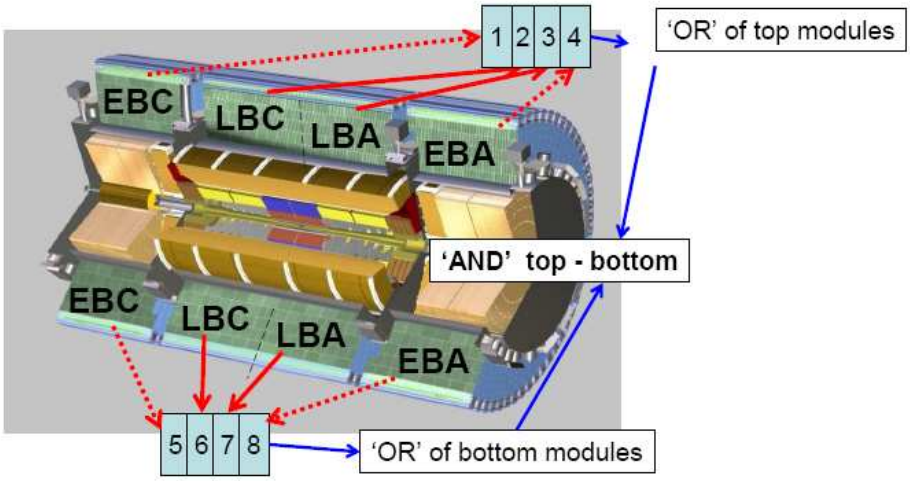

Figure 6.6: Tile trigger setup and logic of the top-bottom coincidence. The extended barrel part EBC was not available for the runs analysed in this analysis.

[1] One trigger tower is the sum of all Tile cells in a region of $\Delta\eta \times \Delta\phi = 0.1 \times 0.1$

Figure 6.7: Cosmic muon event displayed using the Atlantis program crossing the EMEC-A wheel. The Hadronic Calorimeter is in red, while the Electromagnetic Calorimeter is in green. The muon cross from top to bottom depositing energy in both top and bottom EBA Tile towers and in the EMEC-A (small spot in grey).

Chapter 7

Checking signal reconstruction in $|\eta| < 3.2$ with cosmic data

The first cosmic muon data were registered in the ATLAS cavern in August 2006 by the EM barrel calorimeter, in the regions equipped with front-end electronics. First studies focused on these regions (6% of the barrel) and concentrated on projective muon samples [15]. Since March 2007, one end-cap wheel [1] and the whole barrel are fully operational and take data regularly. Focusing on some dedicated cosmic muon runs (taken during "muon" weeks called M3 and M4 afterwards), it is therefore possible to perform a first study on the almost complete calorimeter coverage $-1.4 < \eta < 3.2$. This is particularly suitable to perform an *in situ* test of the signal reconstruction presented in chapter 5. Even with the limited available statistics ($\sim 150\,000$ triggered events), the selection of the few % of events with catastrophic high energy deposits (section 7.1) represents a unique opportunity to perform a first check of the signal reconstruction quality in a coherent way for both barrel and end-cap parts (section 7.2). Finally, section 7.2.3 estimates the impact of the resonance frequency uncertainties on the signal amplitude reconstruction in the end-cap.

7.1 Selection of high energy deposits

Selecting projective muons imposes by default a barrel-restricted analysis. However, considering only events where a hard enough bremsstrahlung photon deposits its energy in the EM calorimeter can allow to perform an analysis in the complete coverage $|\eta| < 3.2$: in this case, the photon induces an electromagnetic shower, detected more easily and

[1] The $z > 0$ side, called ECA wheel. The other side, called ECC wheel, can be integrated in the analyses since M5 period, *i.e.* beginning of November.

independently of the incident muon projectivity. Moreover, this selects "electron-like" energies, of the order of the GeV, which are well suited to test the signal reconstruction procedure.

7.1.1 Conditions of data taking

Since the ATLAS muon trigger was not available on the full coverage (especially in the end-caps) at the time of data taking, a dedicated trigger, using only Tile calorimeter signals, was configured to detect cosmic muons. The available Tile towers, $\Delta\eta \times \Delta\phi = 0.1 \times 0.1$, were asked for a top-bottom coincidence [34] to form the trigger for each data taking period, as shown in Figure 6.6. The compromise between noise and a too low trigger rate results in a ~ 1 GeV threshold per tower and a $\sim 50\%$ muon purity of the triggered events [15].

The main concern in the present analysis is related to the available statistics. This issue is strongly correlated with the trigger set-up. Therefore, even if data are taken nearly every week-end over the whole calorimeter since spring 2007, only runs with stable enough data taking conditions are selected for this analysis (Table 7.1). All data were collected in high gain and $\sim 150\,000$ triggered events are available. It should be noticed that, contrarily to the end-caps, the barrel did not operate under nominal HV but used a reduced value of 1600 V to be better protected from unstable conditions in the cavern. As a consequence, the optimal filtering coefficients were recomputed and the factor converting ADC to MeV was divided by 0.919 [15].

Date in 2007	# of runs (Run #)	Tile Trigger (Figure 6.6)	Triggered Evts ($\times 10^3$)	# of cells with E> 500 MeV (Analysed evts)	
				Barrel	End-cap
29/06-07/07	5 (14066→14848)	EBA	11.2	0 (0%)	490 (100%)
06/10-09/10	6 (23381→24609)	LBA, LBC, EBA	71.4	1276 (52%)	593 (100%)
14/10-16/10	6 (24847→24874)	LBA, LBC, EBA	66.3	1775 (42%)	373 (68%)
Total	17	–	148.9	3051 (44%)	1456 (86%)

Table 7.1: *Characteristics of cosmic runs used in the analysis: run #, trigger set-up, statistics and number of cells with E> 500 MeV (see text for more details). For technical reasons (castor access) and lower statistical limitations, only half of the statistics has been reanalysed for the barrel, whereas almost the complete statistics has been analysed for the end-cap.*

7.1.2 Selection criteria

Unless stated otherwise, the energy is reconstructed with 5 samples OFC [2]. The conversion factor from ADC counts to MeV, presented in Figure 7.1, is computed by factorising the cell gain, $\frac{M_{phys}}{M_{cali}}$, the injected current from the calibration and the sampling fraction. A good agreement is obtained with the foreseen values [35].

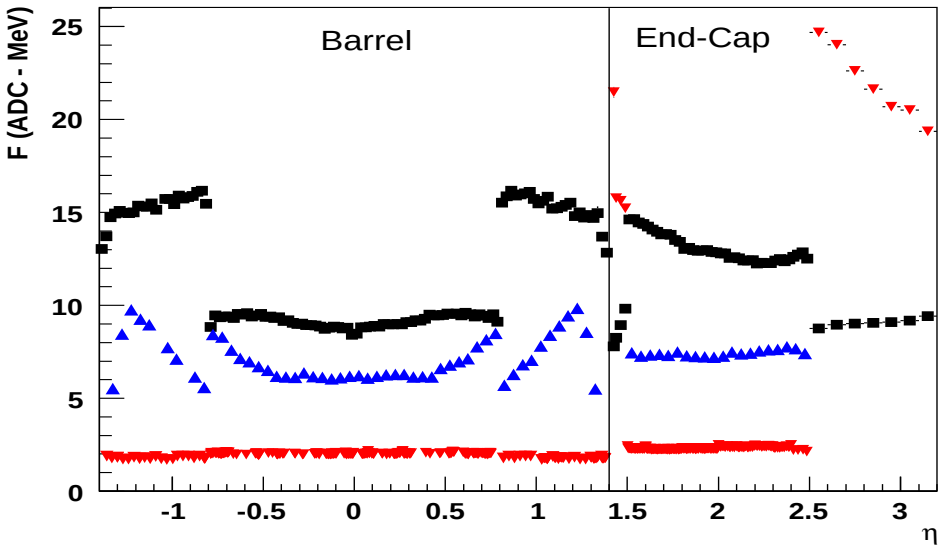

Figure 7.1: *ADC to MeV conversion factor, F(ADC-MeV), as a function of* η *for front (red down triangles), middle (black squares) and back (blue up triangles) cells. All points have been averaged over* ϕ*. High gain and the reference input set of Table 5.1 are used.*

To minimize the fluctuations in the signal reconstruction, the energy deposited per cell should be well above the noise. On the contrary, for statistical reasons, the present analysis can not be performed if the threshold on the energy is too high, and a good compromise is found by requiring $E > 500$ MeV. At this stage, the OFC phase of each cell should be known, *i.e*. the iterative process to determine Δt in Equation (4.2) should have converged ($|\Delta t| < 1$ns). Thanks to the "high" energy cut, more than 99% of the cells fulfill this condition. Failing cases are mainly due to a badly adjusted latency (maximum of the pulse in the first sample).

One of the main difficulty of this analysis is to reject the cells wrongly selected as high energetic cells due to high noise or incorrect pedestal subtraction. A simple and robust criterion to tag this fake cells is to impose that a given cell is selected only once per run, reflecting the very low probability that randomly produced bremsstrahlung photons deposit their energy in the same cell twice per run. As only high gain is available, cells

[2] The same calibration constants (pedestal, autocorrelation matrix, ramp) are used for all runs.

with more than 2500 ADC counts [3] after pedestal subtraction are also rejected to avoid saturation effects. After this selection, ∼1500 cells are selected in the end-cap and ∼3000 in the barrel (Table 7.1).

7.1.3 Map of selected cells

The mapping of the selected cells is presented in Figure 7.2 in the front-end electronic boards (FEB) coordinates, and Figure 7.3 in the $\eta - \phi$ plane for each layer. In both barrel and end-cap, the statistics is almost equally spread in each FEB slot corresponding to the second layer [4]. The increase in top and bottom regions [5], due to the down-going cosmic direction, is clearly visible.

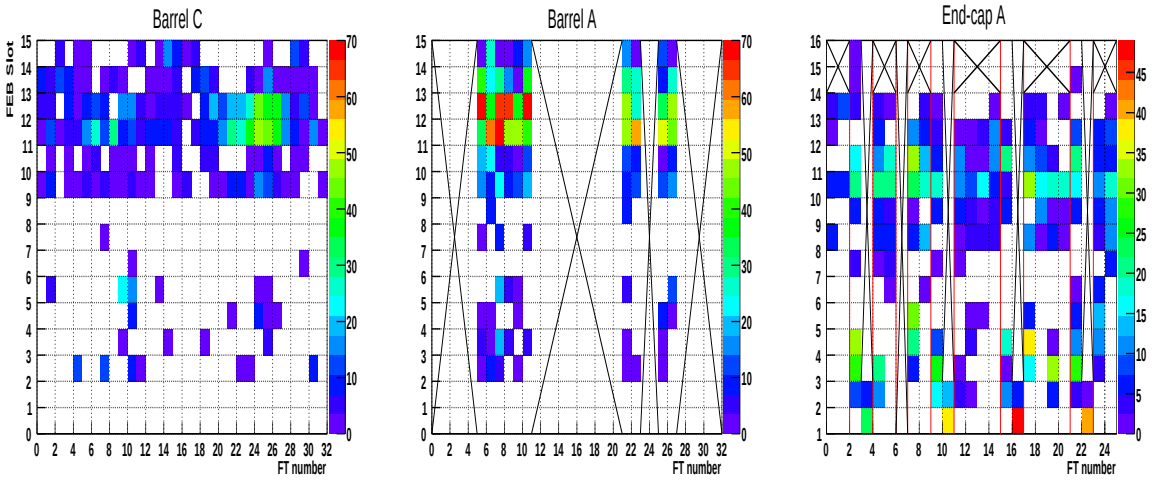

Figure 7.2: *FEB slot - Feedthrough (FT) number mapping of high energetic cells in the barrel C (left), A (middle) and end-cap A (right). Crosses indicates the unplugged electronics in the barrel and empty slots or HEC/FCAL slots in the end-cap.*

The energy distribution of the selected cells is shown in Figure 7.4 for the three layers of the barrel (left) and the end-cap (right). In the barrel, 80% of the statistics is concentrated in S2, the rest being shared between S1 and S3. In the end-cap, S2 cells represent only $2/3^{rd}$ of the statistics, because of the non-projective situation (the photon sees the cell size in the $\eta - \phi$ plane and not the cell depth). The average energies of all distributions are around 1.5 GeV. It can be noticed that, given the small η size of S1 cells,

[3] This corresponds roughly to 6 GeV in S1, 35 GeV in S2 and 17 GeV in S3. (CHECK)

[4] FEB slot $\geq 11(10)$ in the barrel (standard end-cap) crates. In special (HEC) crate FT 2, 9, 15, 21 (3, 10, 16, 22) it corresponds to slot number 3, 4, 10, 11, 14, 15 (2).

[5] FT 5-10 (4-8) and 21-26 (17-20) for top and bottom in the barrel (end-cap).

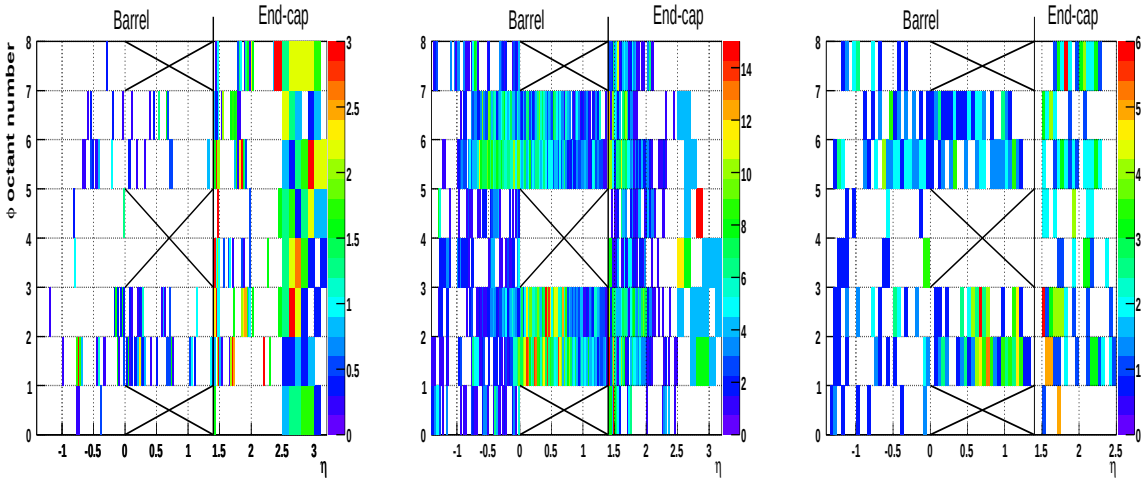

Figure 7.3: $\eta - \phi$ *map of high energetic cells in S1 (left), S2 (middle) and S3 (right) for* $|\eta| < 3.2$. *Crosses indicates the unplugged electronics in the barrel and empty slots or HEC/FCAL slots in the end-cap.*

the selection generally involves a group of cells per event, rather than isolated cells like in S2 or S3, as seen in Figure 7.3. This is illustrated in Figure 7.5, where a high energetic shower (E$>$ 200 GeV) illuminates more than 50 S1 cells at $\eta \sim 1.8$.

7.2 Comparison of predicted physics pulse shapes with data

This section presents the first check of the signal reconstruction performed over the full calorimeter coverage. The method is first explained, and the pulse shape predictions are then systematically and quantitatively compared to the cosmic data. Finally, a focus is made on the drift time impact.

7.2.1 Method to superimpose predictions and data

To compare the predicted physics pulse shapes (normalized to one) with the data for all selected cells, the first step is to multiply the prediction by the maximum amplitude computed for each cell. Because of different FEB timings and asynchronous muon arrival times, a global time shift is then determined for each cell by minimizing the following χ^2

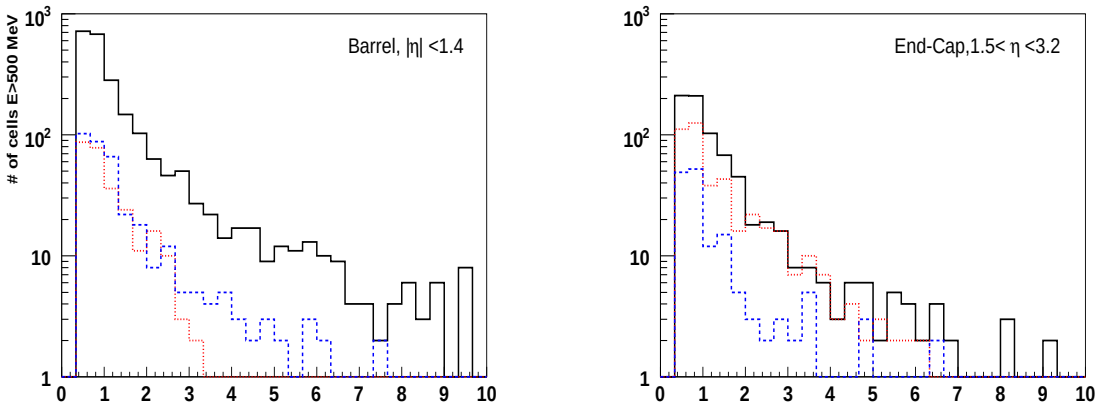

Figure 7.4: *Energy distribution of selected cells in the barrel (left) and in the end-cap (right). S1, S2 and S3 cells are represented with red dotted, black full and blue dashed histograms.*

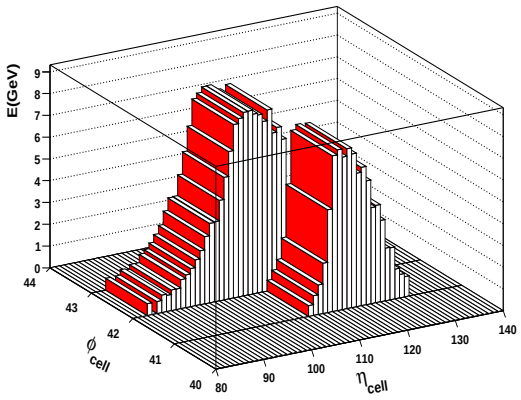

Figure 7.5: η-ϕ *mapping of a high energy shower (>200 GeV) in S1 at* $\eta \sim 1.8$. *In this event 56 cells are above 500 MeV and 18 above the saturation threshold (∼6 GeV).*

through an iteration by steps of 25 ns :

$$\chi^2 = \sum_{i=1}^{n} \left(\frac{A_i^{data} - A_{max} * g_i^{phys}}{\sigma_{noise}} \right)^2 \tag{7.1}$$

where n is the number of samples considered, A_i^{data} is the amplitude of each sample i in ADC counts for data, A_{max} is the maximum amplitude defined in Equation (4.6) and g_i^{phys} the predicted physics pulse shape defined in Equation (4.2). Finally, σ_{noise} corresponds to the noise for a single sample in ADC counts [6].

After this time adjustment, data and predictions can be compared. Figure 7.6 shows typical physics shapes for each sampling (S1, S2 and S3 from top to bottom) in the barrel (left) and in the end-cap (right). For 5 sample pulse shapes, the predictions agree nicely with the data in the raising and falling edges of the pulses. More quantitative conclusions are drawn in section 7.2.2. For 25 samples, apart from the systematic bias observed around the maximum, a fair agreement is visible in the falling edge and in the undershoot, except for the highest sample numbers, which was already reported in [15]. A more quantitative discussion on these points is proposed in section 7.2.4.

[6] Approximately, 9/3/6 ADC counts in S1/S2/S3 for $|\eta| < 2.5$ and 6/5 ADC counts in S1/S2 for $|\eta| > 2.5$.

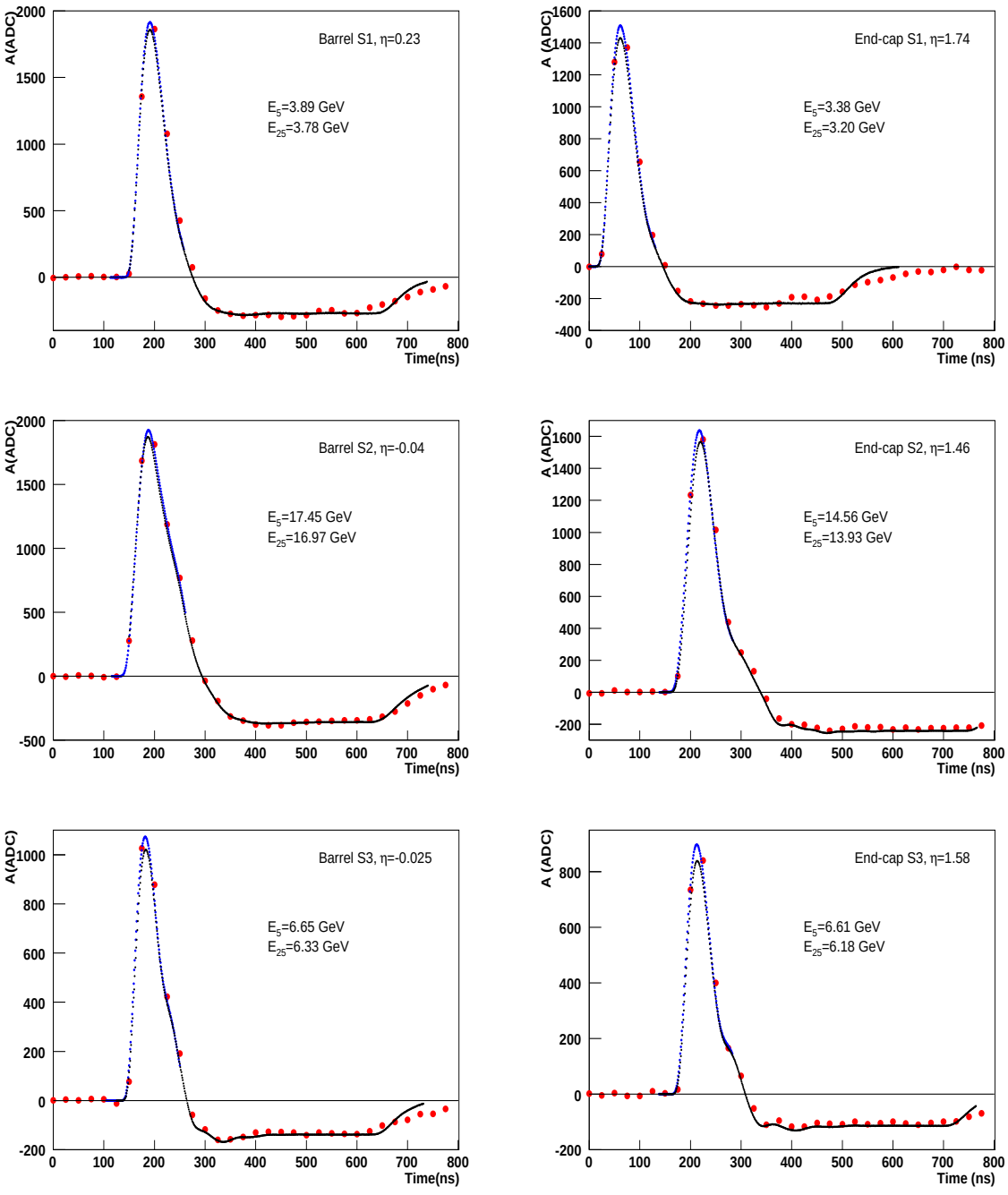

Figure 7.6: *Typical cell response in high gain to high energy deposits in the barrel (left) and end-cap (right) layers (S1, S2 and S3 from top to bottom). The blue (resp. black) curves correspond to the predicted pulse shapes using 5 (resp. 25) samples.*

7.2.2 Quality of the predicted pulse shapes

The χ^2 proposed in Equation (7.1) can also be used to perform a systematic quantitative comparison between data and pulse shape predictions over the full η coverage. By construction, this estimator of the prediction quality depends on the square of the energy. To allow a comparison between barrel and end-cap, whose energy spectra per layer are different (Figure 7.4), it is divided by the square of the reconstructed amplitude, ${A_{max}}^2$. Moreover, only 5 samples ($n = 5$) are considered, as this is what will be used to reconstruct the energy in ATLAS. The comparison with 25 samples will be presented in section 7.2.4.

Results for this estimator of the data/prediction comparison, $\chi^2/{A_{max}}^2$, are shown in Figure 7.7 as a function of the energy for the three layers in the barrel (left) and in the end-cap (right). It is fitted by the following simple function, which allows a very good modeling in all layers of the barrel and end-cap parts :

$$\frac{\chi^2}{n_{samples} \times {A_{max}}^2} = \frac{p_0}{E^2} + p_1 \tag{7.2}$$

The first term, dominating at low energy, is due to the gaussian noise fluctuation for each sample. It is hardly visible in S1, as the noise in this sampling is lower and already negligible for a 500 MeV energy deposit. The second term, dominating at high energy where the noise contribution can be neglected, reflects the quality of the predicted shape as compared with the data. The results are only slightly better in the barrel compared to the end-cap. This is the first proof of the quality of an ATLAS-like signal reconstruction in the end-caps, despite its challenging aspect. This is also illustrated in Figure 7.8, which shows the pulse shape prediction quality $\chi^2/{A_{max}}^2$ as a function of η between 0 and 3.2 for the three samplings [7]. These results are obtained by applying a lower energy cut (0.5, 1.5 and 1.2 GeV in S1, S2 and S3 respectively), to minimize the noise contribution, and an upper cut (2500 ADC counts) to avoid high gain saturation. Again, a smooth behavior is obtained with only slight differences between barrel and end-cap. This assesses the coherence of the signal reconstruction quality, using 5 samples as foreseen in ATLAS, over the complete calorimeter coverage $0 < \eta < 3.2$.

It is finally worth mentioning that the computation of the χ^2 proposed in Equation (7.1) will be performed *on-line* above a given energy threshold in the Read-Out Driver modules [36], to control the quality of the signal reconstruction in all cells. This will be useful to mask the most problematic channels, as it was done in this analysis : a few cells exhibiting a too large χ^2 have been removed from Figures 7.7 and 7.8. The reasons leading to these bad physics shape data will be investigated.

[7] The absolute values of the quality estimator depend on the injection resistors, which are different between samplings.

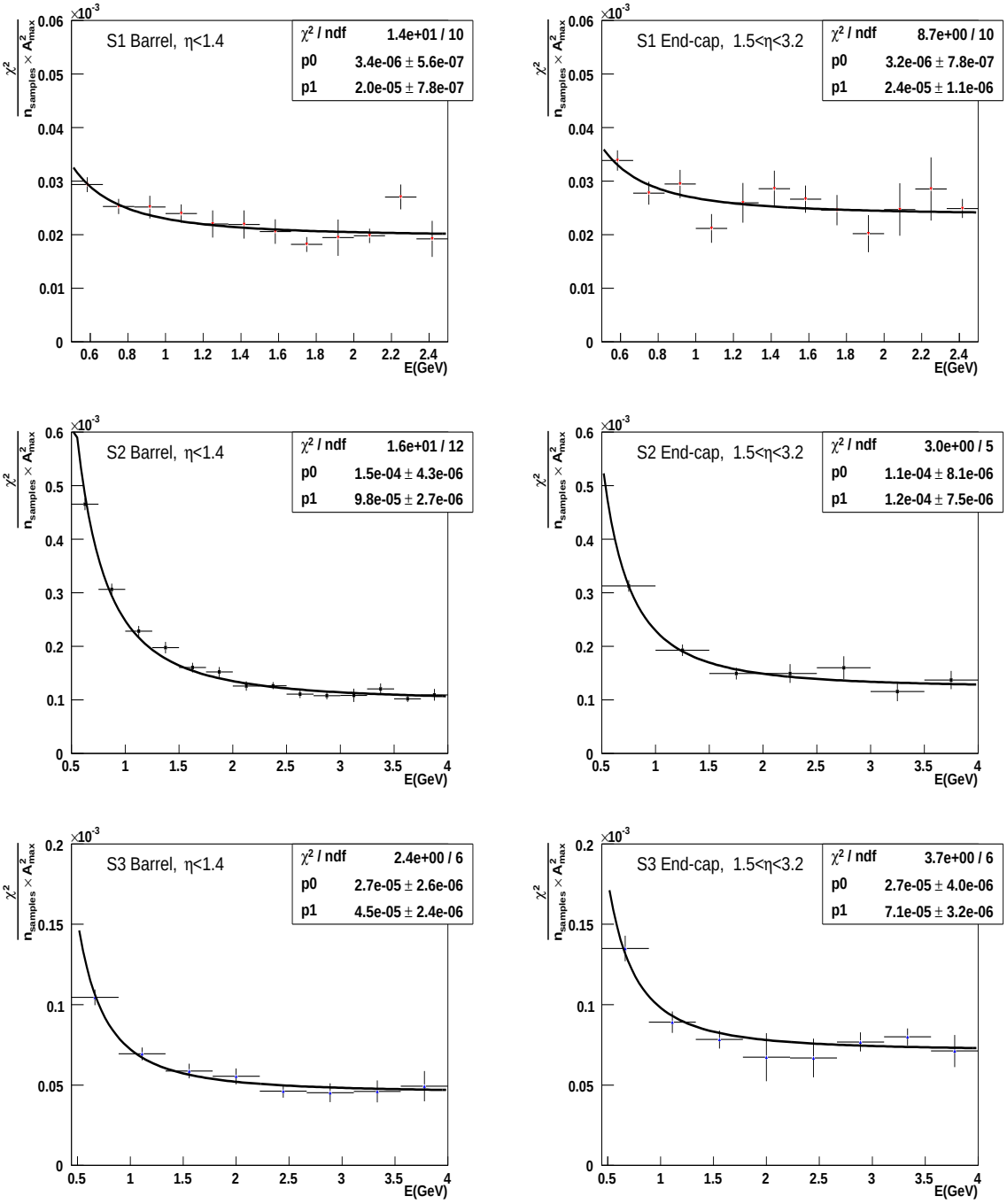

Figure 7.7: *Estimator $\chi^2/{A_{max}}^2$ of the quality of the predicted physics pulse shape as a function of the energy for the barrel (left) and the end-cap (right) in S1, S2 and S3 (top to bottom). 5 samples and high gain are used. The function used for the fit corresponds to Equation (7.2).*

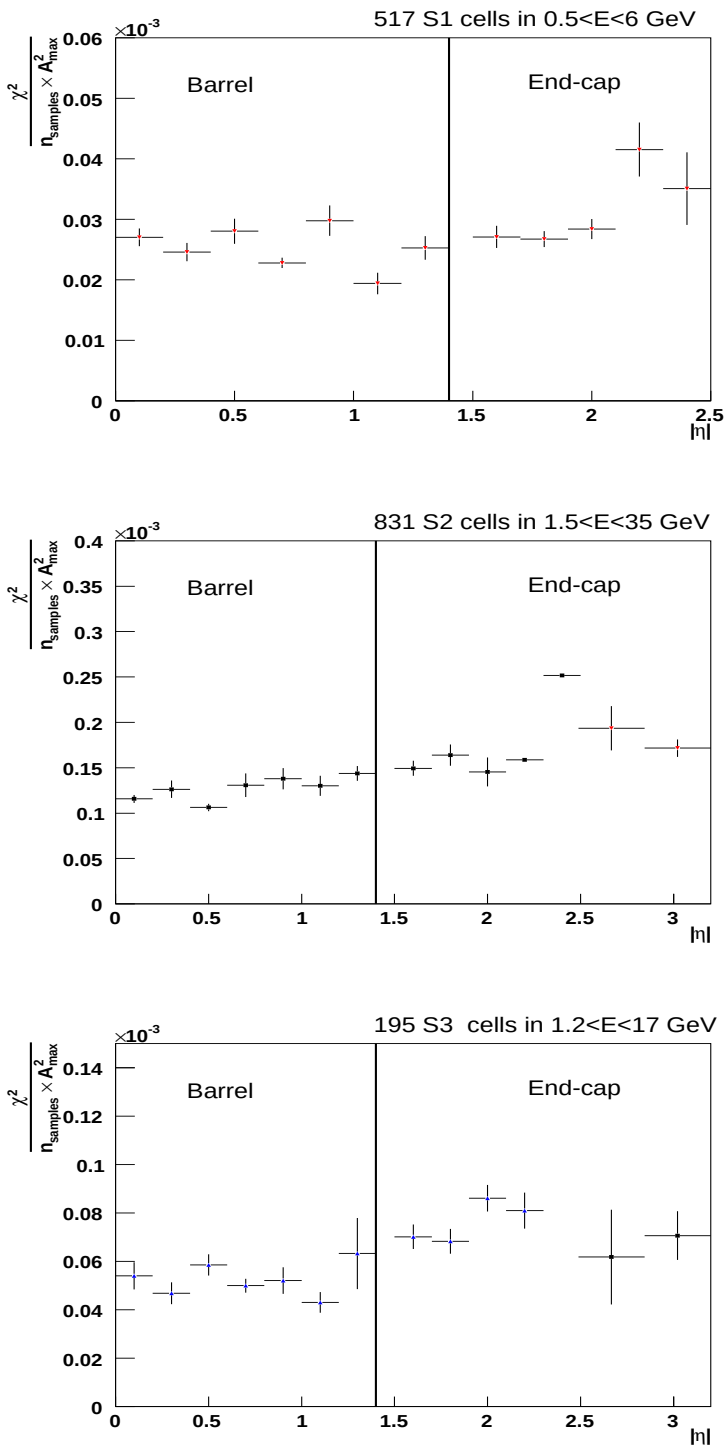

Figure 7.8: *Estimator $\chi^2/A_{max}{}^2$ of the quality of the predicted physics pulse shape as a function of $|\eta|$ for S1 (left), S2 (center) and S3 (right). 5 samples and high gain are used.*

7.2.3 Main systematic uncertainty in the end-cap signal reconstruction

The main uncertainty from the input parameters concerns the resonance frequency values ω_0, for which the disagreement between different measurement methods can reach up to 10-15% (section 5.1.4). To estimate quantitatively the impact of this uncertainty on the energy reconstruction, two sets of optimal filtering coefficients have been built (reference set and set 2 of Table 5.1). The relative difference between energies reconstructed with these two sets is shown in Figure 7.9(a) as a function of the relative ω_0 difference. A linear dependence is fitted, with an energy bias around 0.05% per percent of ω_0 variation [8]. At maximum (15% uncertainty on ω_0), the related systematic uncertainty on the energy is of the order of 0.5%.

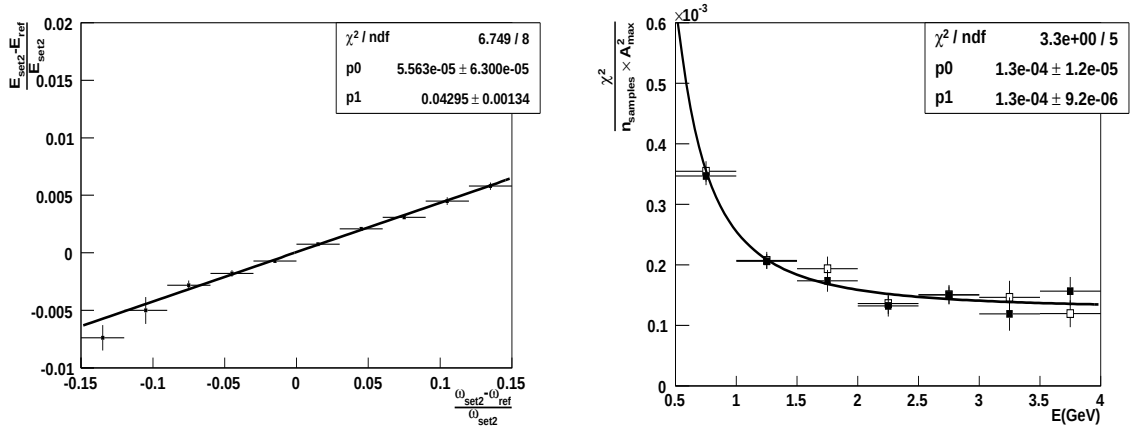

(a) (b)

Figure 7.9: *(Left): relative difference between energies reconstructed with the two sets of optimal filtering coefficients, as a function of the relative difference between their input resonance frequencies. A linear fit is superimposed. (Right): Estimator $\chi^2/{A_{max}}^2$ of the quality of the predicted physics pulse shape for S2 in the end-cap, as a function of the energy, for the two sets of optimal filtering coefficients (closed symbols for reference set and open symbols for set 2). The fit is performed on the data from the second set.*

Trying to use cosmic data to discriminate between both sets of OFC for the end-caps, the study comparing data and pulse shape predictions presented in section 7.2.2 has been done using both sets of ω_0 values. The estimator of the pulse shape prediction quality, $\chi^2/{A_{max}}^2$, is shown for S2 in Figure 7.9(b) as a function of the energy for

[8] This is in good agreement with [11], which reported a $\sim 0.05\%$ amplitude variation for a 1% ω_0 variation in the barrel.

both sets. No significant differences are found within the available statistics, which is too low to perform a η-dependent analysis. High p_T isolated electrons from LHC data will be mandatory to go further and improve the ω_0 knowledge below 5%, reducing the systematic error on the energy to less than 0.2%.

7.2.4 Influence of the ion drift time on the pulse shape description

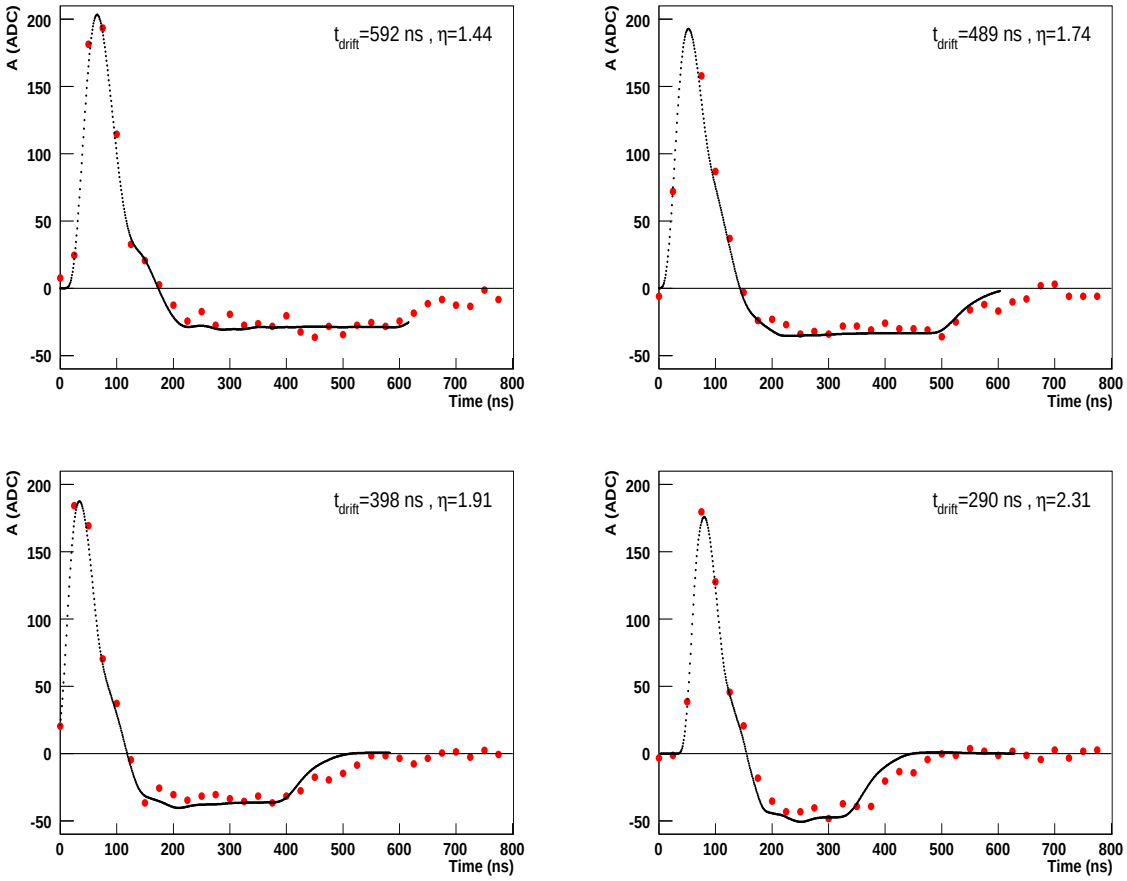

Figure 7.10: *Typical S2 cell responses in high gain to high energy deposits in the end-cap at different* η *values. The black curves correspond to the predicted pulse shapes using 25 samples. For each* η*, the ion drift time, reflected in the undershoot duration, is indicated.*

The previous sections focused on the quality of the pulse shape prediction with 5 samples, that will be used to reconstruct the energy in ATLAS. The inspection of the pulse part between the 5^{th} and the 25^{th} samples, including the negative undershoot, allows to

go one step further, as it permits to investigate in more details the quality of the input parameters needed to predict the shape. For instance, the undershoot duration is directly linked to the drift time. This is illustrated in Figure 7.10, where typical cell responses are superimposed to the 25 samples predicted pulse shapes. For increasing η, the reduction of the undershoot duration due to the steep decrease of the ion drift time (Figure 5.3) is clearly visible.

As a consequence, the description of the part of the pulse shape after the 5^{th} sample is more difficult, especially in the end-cap. This is also clearly seen in Figure 7.10, where the undershoot prediction is systematically below the data. This induces a bias on the amplitude reconstruction when a large number of samples is used [9]. To quantify this bias, Figure 7.11 (left) shows the relative difference between energies reconstructed with 25 or 5 samples in the barrel (open symbols) and in the end-cap (closed symbols). As expected, the bias is independent on the energy. It is around -3% in the barrel, in good agreement with what has already been reported in [15]. This is almost double in the end-cap, reflecting the difficulty to keep completely under control the steep variations of the signal reconstruction input parameters over the η-coverage (section 5). This is also seen in Figure 7.11 (right) that shows the bias from pulse shape residuals as a function of η. Flat in the barrel, as expected, the bias is reduced for increasing η in the end-cap outer and inner wheels. This reflects the decrease of the undershoot duration, which lowers its impact on the reconstructed energy.

As discussed above, a precise determination of the drift time variation along η could improve the pulse pulse shape description between the 5^{th} and the 25^{th} samples. In the end-cap, the previous measurements were obtained by fitting 125 ns physics pulse shape in electron beam tests with a $\sim 10\%$ precision (section 5.1.3). It is therefore interesting to extract the drift time from cosmic data looking at the 800 ns shapes. This can be done either by measuring the undershoot duration, or its relative height amplitude.

The undershoot duration is estimated by computing the difference between the time of the first sample with negative amplitude (or the sample with absolute amplitude below -2σ of the noise) and the first sample with positive amplitude after the undershoot (or the sample with absolute amplitude above -2σ of the noise). The latter may not exist for cells with high drift time values or for prediction with 25 samples (see Figure 7.6), and 32 samples are therefore used for this exercise. However, the measurement with data is spoiled by the low statistics of events with high enough energies and the associated time jitter, preventing an accurate determination of the drift time. The latter can also be

[9] By construction, positive and negative areas of the pulse are equal.

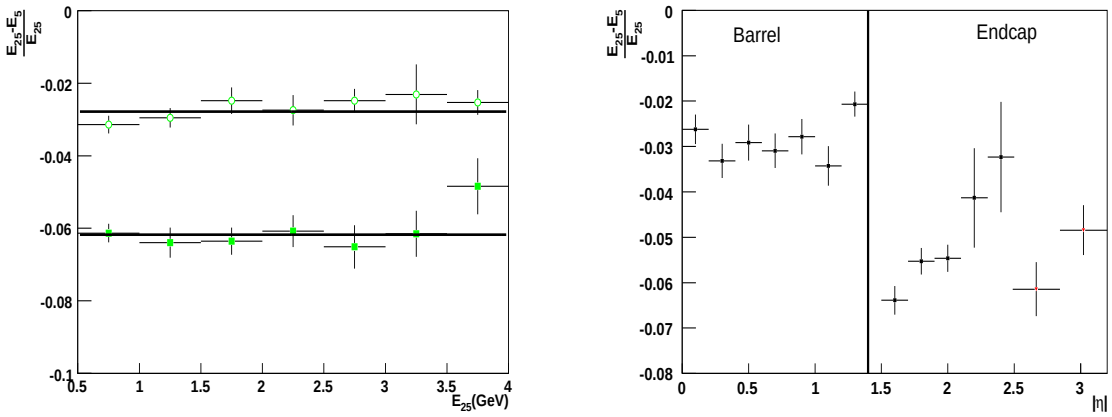

Figure 7.11: *Relative energy difference between reconstruction with 25 and 5 samples in S2 as a function of the energy reconstructed with 25 samples (left) and as a function of* η *(right). In the left plot, open (closed) symbols represent barrel (end-cap), and* p_0 *is the result of a fit with a constant value.*

correlated to the relative height amplitude of the undershoot *r* :

$$r = \frac{A_{max}^{OFC_{5s}} + |\frac{1}{n}\sum_{i=1}^{n} A_{min}^{i}|}{A_{max}^{OFC_{5s}}} \tag{7.3}$$

where $n = 5$ is the number of samples used to estimate the average of the undershoot height [10]. Figure 7.12 shows *r* as a function of the input drift time in the end-cap and in the barrel, as obtained with data and with the predicted physics pulse shapes. The barrel *r* value is higher than for the end-cap, reflecting the shape difference in the falling edge (between the 5^{th} and the 9^{th} samples) observed in Figure 7.6, which is linked to different capacitance values and signal cable lengths. In the end-cap, a linear behavior between *r* and the input drift time is observed, both for data and predictions. Data derived *r* values are systematically lower than those from the pulse shape prediction. This suggests that the input drift time has been systematically underestimated, as already inferred from Figure 7.10. However, the statistics is too poor to deconvolute all second order effects (electric field variation with η, *LC* dependence, non-projectivity of energy deposits, ...) and extract an enough accurate measurement usable for the signal reconstruction.

[10] The sample A_{min}^{1} is located 50 ns after the first sample with negative amplitude.

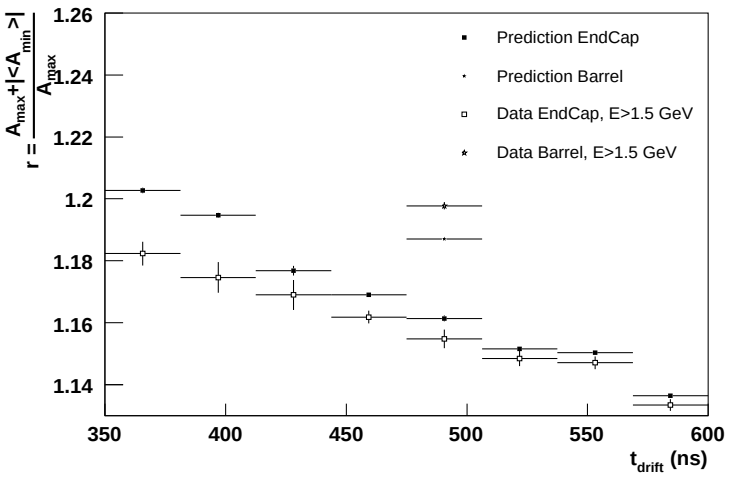

Figure 7.12: *Relative height amplitude of the undershoot r (see text) as a function of the input drift time in S2 for the barrel and the end-cap. Values derived from data and from predicted physics pulse shapes are shown. To lower the noise contribution, an energy cut* $E > 1$ *GeV (section 7.2) is applied.*

Chapter 8

Conclusions

As part of the calibration procedure of the ATLAS Electromagnetic Calorimeter, Optimal Filtering Coefficients have been computed for all channels of the End-Cap Electromagnetic Calorimeter (EMEC), to be used in any physics analysis to obtain the energy in calorimeter cells. This computation needs the knowledge of the response pulse shape to ionization (physics).

This shape has been predicted from the calibration pulse shape, using the RTM method to determine some electrical properties of the calibration system and of the calorimeter cells. This is the first time this procedure is applied to the EMEC. The quality of the prediction has been checked using cosmic muon data.

For the first time, a complete analysis of cosmic muons has been performed for the whole EM Calorimeter, barrel and End-Caps, selecting those muons with high energy deposits. A good agreement between the predicted pulses and the muon data pulses have been found for the 4500 cells analysed in the whole EM Calorimeter, almost 1500 of them in the EMEC.

This is the first proof of the quality of an ATLAS-like signal reconstruction in the end-caps, despite its challenging aspect (more complicated geometry and η-dependence electrical parameters), and gives confidence that the energy reconstruction is in good control over the complete calorimeter coverage $-3.2 < \eta < 3.2$.

Bibliography

[1] P. Lefevre and T. Pettersson, *The Large Hadron Collider: conceptual design*, CERN-AC-95-05-LHC, 1995.

[2] ATLAS/Inner Detector Collaboration, *Inner Detector Technical Design Report*, CERN/LHCC 97-16, 1997.

[3] ATLAS/Liquid Argon Calorimeter Collaboration, *Liquid Argon Calorimeter Technical Design Report*, CERN/LHCC 96-41, 1996.

[4] ATLAS/Tile Calorimeter Collaboration, *Tile Calorimeter Technical Design Report*, CERN/LHCC 96-42, 1996.

[5] ATLAS/Muon Spectrometer Collaboration, *Muon Spectrometer Technical Design Report*, CERN/LHCC 98-14, 1998.

[6] O. Martin, E. Monnier, S. Tisserant; *Update of some Geometrical Parameters for the ATLAS EM End-Cap Calorimeter*, ALTAS-LARG-NO-47 (1996)

[7] Donald H. Perkins, *Introduction to High Energy Physics*, 4th Edition, 349-351.

[8] Davis J. Griffiths, *Introduction to Electrodynamics*, 3rd edition, pages 463-464 .

[9] William R. Leo, *Techniques for Nuclear and Particle Physics Experiments*, Published 1994, Springer.

[10] W.-M. Yao et al., *Review of Particle Physics*, J. Phys. G33,1 (2006).

[11] D. Banfi, M. Delmastro and M. Fanti, *Cell response equalization of the ATLAS electromagnetic calorimeter without the direct knowledge of the ionization signals*, SN-ATLAS-2005-054, J. Inst **1** (2006) P08001.

[12] M. Aharrouche *et al.*, *Energy linearity and resolution of the ATLAS electromagnetic barrel calorimeter in an electron test-beam*, Nucl. Inst. Meth. **A 568** (2006) 601.

[13] J. Colas *et al., Response Uniformity of the ATLAS Liquid Argon Electromagnetic Calorimeter,* Nucl. Inst. Meth. **A 582** (2007) 429, arXiv:0709.1094 [physics].

[14] M. Aleksa *et al., ATLAS Combined Testbeam : Computation and Validation of the Electronic Calibration Constants for the Electromagnetic Calorimeter*, ATLAS note ATL-LARG-PUB-2006-003.
D. Goldin and M. Delmastro, *On the feasibility of predicting the ATLAS EM Calorimeter ionization signals using the Time Convolution Method at the LHC sampling rate*, ATLAS note ATL-LARG-PUB-2007-004.

[15] M. Cooke, P.S. Mangeard, M. Plamondon *et al., In situ commissioning of the ATLAS electromagnetic calorimeter with cosmic muons*, ATLAS note ATL-LARG-PUB-2007-013.

[16] The ATLAS Collaboration, *Liquid Argon Calorimeter, Technical Design Report*, CERN/LHCC/96-41.

[17] B. Aubert *et al., Construction, assembly and tests of the ATLAS electromagnetic barrel calorimeter,* Nucl. Inst. Meth. **A 558** (2006) 388.

[18] M. Aleksa *et al., Construction, assembly and tests of the ATLAS electromagnetic end-cap calorimeter*, submitted to J. Inst.

[19] W.E. Cleland et E.G. Stern, *Signal processing considerations for liquid ionization calorimeter in a high rate environment,* Nucl. Inst. Meth. **A 338** (1994) 467.

[20] C. Collard *et al., Prediction of signal amplitude and shape for the ATLAS electromagnetic calorimeter*, ATL-LARG-PUB-2007-010.

[21] F. Hubaut *et al., Crosstalk in production modules of the Electromagnetic Endcap Calorimeter,* ATLAS note ATL-LARG-2003-012.

[22] S. Baffioni *et al., Electrical Measurements on the ATLAS electromagnetic barrel calorimeter*, ATLAS note ATL-LARG-PUB-2007-005.

[23] Lydia Fayard, *Hardware measurements of Rcal and LC in barrel*, presentation at EM calibration workshop, Annecy, october 2007.

[24] J. Colas, *Calibration and non ideal calibration cables*, presentation at EM electronics calibration, BNL, May 2007.

[25] Marco Delmastro, *How to compute optimal filtering coefficients*, presentation at EM calibration workshop, Annecy, October 2007.

[26] C. de La Taille and L. Serin *Temperature dependance of the ATLAS electromagnetic calorimeter signal. Preliminary drift time measurement*, ATLAS note LARG-NO-29.

[27] B. Aubert *et al.*, *Performance of the ATLAS Electromagnetic Calorimeter Endcap Module 0*, Nucl. Inst. Meth. **A 500** (2003) 178.

[28] F. Hubaut and C. Serfon, *Response uniformity of the ATLAS electromagnetic endcap calorimeter*, ATLAS note ATL-LARG-2004-015.

[29] C. Oliver and J. del Peso, *Outer Wheel Uniformity of the Electromagnetic EndCap Calorimeter*, ATLAS note ATL-LARG-PUB-2005-002.

[30] P. Barrillon et al., *Electrical tests for the validation of the electromagnetic end-cap calorimeter modules*, ATLAS note ATL-LARG-2003-004.

[31] F. Djama, *Using $Z^0 \rightarrow e^+e^-$ for Electromagnetic Calorimeter Calibration* , ATLAS-2004-008.

[32] Lydia Fayard, *Comparison between different ionisation pulse predictions*, presentation at EM electronics calibration meeting, LAr Week, November 2005.

[33] C. Gabaldon, *Check OFC using Pedestal runs* , presentation at BP3C meeting, 30/08/2007.

[34] K. Anderson, J. Pilcher, H. Sanders, F. Tang, and R. Teuscher, *Stand-alone Cosmic Ray Trigger Electronics for the ATLAS Tile Calorimeter*, Proceedings, 10th Workshop on Electronics for LHC and Future Experiments, September 13-17, 2004, Boston, USA.

[35] W. Lampl *et al.*, *Digitization of LAr calorimeter for CSC simulations*, ATLAS note ATL-LARG-PUB-2007-011.

[36] J. Ban *et al.*, *ATLAS liquid argon calorimeter back end electronics*, J. Inst **2** (2007) P06002.

[37] Marco Delmastro, *Quality factor analysis and digital filtering optimization*, EM electronics calibration meeting, LAr Week, December 2007.